Theoretical Analysis of α-Actin Stability at High Pressure

Nobuhiko Wakai

Student ID: 47-096913

Department of Computational Biology

Graduate School of Frontier Sciences

The University of Tokyo

Supervisor: Akio Kitao

Abstract

The main component of muscle fiber is α-actin, which plays many important roles in cellular functions. Monomeric actin protein can polymerize into filament with ATP hydrolysis. The amino acid sequences of actins are known to be highly conserved in many species. Deep-sea fish actins have the specific substitutions, Q137K/V54A or Q137K/L67P. Since only Q137K substitution is located near the active site, this residue is expected to contribute to the pressure tolerance. Although some experiments showed the effects of substitutions at high pressure, the detailed mechanism of pressure tolerance induced by substitutions is still unclear, especially in molecular level. Using the molecular dynamics simulations of various actins, I analyzed high pressure effects on actin structures and dynamics. In deep-sea fish actins, the number of salt bridges increases and several salt bridges specific to deep-sea fish actins are observed. The salt bridge between Lys-137 and ATP in deep-sea fish actins stabilizes ATP binding at the active site under high pressure. Other deep-sea specific salt bridges mostly connect pairs of secondary structures and subdomains. The salt bridges which deep-sea fish have are suggested to be a key for the mechanism of the pressure tolerance.

Contents

1 Introduction

Actin plays many important roles in numerous cellular functions in muscle and nonmuscle cells. The amino acid sequences of actins are known to be highly conserved in many species. Actins are mainly categorized into three isoforms as α-, β-, and γ-actins. Vertebrate actin can be farther classified into six isoforms: α-skeletal actin, α-vascular actin, and α-cardiac actin; β-nonmuscle actin; γ-smooth actin and γ-nonmuscle actin [1]. The main component of muscle fiber is α-actin, which is one of the most abundant proteins. α-actin forms stable filaments and connects myosin filaments in sarcomeres whereas unstable actin filaments are polymerized and depolymerized as motor proteins, especially filopodia and lobopodia [2]. Most of α-actins are related to dynamics and stability of cell. Some nonmuscle cells have β-actin as either globular actin (G-actin) or filamentous actin (F-actin) to maintain their structures. Basically, β-actin is known as a structural protein. However, it is also involved in a signaling molecule to regulate synthases [3]. The large number of β-nonmuscle and γ-nonmuscle actins exists in every mammalian cell [4]. Although both of them are similar protein, their four amino acid residues are different and these actins are differentially localized [5]. In addition, they are treated with different post-translational modifications [6].

Although the first crystal structure of G-actin was solved in 1990 [7], it is difficult to solve the structure of F-actin at high resolution. However, some structures were solved using the cryo-electoron microscopy recently [8; 9; 10; 11]. Through the comparison between G- and F-actin, the difference in these conformations was analyzed. The experiments showed that the active site

biding nucleotide separates two major actin domains which consist of subdomain 1 and 2 at the outer filament and subdomain 3 and 4 at the inner filament [7]. In addition, a covalent cation and nucleotide such as ATP or ADP exist at the center of G-actin (Figure 1). The divalent cation was coordinated by oxygen atoms of phosphate in the nucleotide.

Table 1. Relationship of α-actin subdomains and residues [12].

Subdomain	Residue
1	1-32, 70-144, 338-375
2	33-69
3	145-180, 270-337
4	181-269

Among four subdomains, subdomain 2 is the most flexible. In particularly, subdomain 2 has highly flexible loop and it can bind proteins like DNase I [7]. Other parts of actin also interact with many actin-binding proteins such as profilin or cofilin [13; 14]. These proteins affect actin conformations and then the rate of polymerization is accelerated or decelerated.

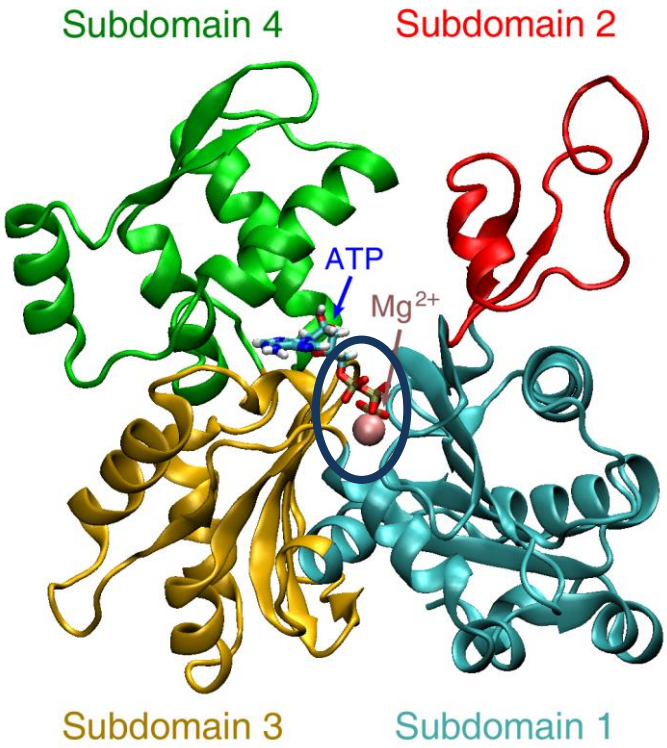

Figure 1. A snapshot of *Coryphaenoides yaquinae* actin 2b (600 bar) after 70-ns molecular dynamics simulations. This actin structure indicated by new cartoon model is colored using subdomain numbers. The navy blue circle denotes the active site. The figure was generated using VMD [15].

G-actin is only polymerized in the salt condition such as $MgCl_2$ or $CaCl_2$ with ATP hydrolysis because the catalytic activation needs a divalent cation assist [16]. F-actin has the orientation and the barbed end is more elongated than the pointed end [17]. These about three actins at the barbed end bind ATP at the active site whereas other parts of the filament consist of actins with ADP. When G-actin binding ATP contacts the end of filament, it starts changing the conformation. Through the rotation like a propeller between subdomain 2 and 3, G-actin becomes a more flat conformation whereas G-actin is twisted by about −20° in general. The flat conformation actin is

less stable than the twisted conformation which G-actin has. However, the flat conformation is appropriate to contact other F-actin and the total energy of flat conformation is lower than the twisted G-actin [8]. During the elongation of the filament, ATP binding F-actin is hydrolyzed to ADP slowly. In particularly, the pointed end of the F-actin binding ADP is depolymerized and then ADP is released. Through the polymerization and depolymerization, the length of the filament is elongated, maintained, or dwindled depending on cellular functions. When the rate of polymerization and depolymerization are equal, the length of filament is not changed; this condition is called treadmilling [17]. Although the length does not change in treadmilling, the position of the filament moves to perform cell motility.

Denaturation, conformational changes, and loss of the enzyme activities of proteins were observed to be induced by high pressure experiments [18; 19; 20; 21]. In addition, the ligand dissociating rate of hydrolases and dehydrogenases was shown to increase at high pressure [20; 22; 23]. Pressure effect on actin was first measured in 1966 [19].The denaturation induced by pressure started at 2500 bar and then pressure induced the completely denaturation for rabbit G-actins at 4000 bar [19]. In addition, pressure prevents G-actin from assembling due to denaturation or conformation changes. High pressure has been shown to induce significant effects on the actins purified from land or shallow water species, which are observed as decrease of DNase I inhibiting, decrease of volume change at polymerization, increase of critical concentration, and increase of the dissociating rate for ligands [20]. Some creatures like deep-sea fish can live under the sea whose depth is about up to 6000 m and the pressure reaches 600 bar. Many researchers used marine

fish which live in widespread depth to study pressure tolerance. One of the best fish for experiment is *Coryphaenoides* known as rattail or grenadier for experiments. Three different fish belonging to *Coryphaenoides* are known; *C. acrolepis* inhabiting in 180-2000 m, *C. armatus* in 2700-5000 m, and *C. yaquinae* in 4000-6400 m. The amino acid sequences of these three fish α-actins are known to be highly conserved and other species living land or shallow water also have similar sequences [20; 21]. Only deep-sea fish actins have Lys-137 near the active site and other species have a glutamine in this position. These residues affect the reaction of hydrolysis and are expected to be one of the key residues in polymerization. Previous study suggested that the residue played an important role in controlling water molecules which behave as nucleophiles attacking ATP [24]. Probability of attacking ATP by water molecules can dominate the rate of polymerization [25]. In addition to Q137K substitution, deep-sea fish actins have substitutions either L67P or V54A. Both L67P and V54A are located on protein surface and quite separated from the active site. Among these substitutions, Q137K near the active site of hydrolysis is expected to play essential role on the pressure tolerance of ligand binding.

Table 2. Comparison of the amino acid sequences of deep-sea fish and species living in land or shallow water.

Actin	Residue									
	2	3	54	67	137	155	165	278	299	358
C. acrolepis actin 1	D	E	V	L	Q	A	V	A	L	S
C. acrolepis actin 2a	D	E	V	L	Q	S	V	A	L	S
C. armatus actin 2b*	D	E	A	L	K	S	V	A	L	S
C. yaquinae actin 2b*	D	E	V	P	K	S	V	A	L	S
Carp	D	D	V	L	Q	A	V	A	L	T
Rabbit / Chicken	E	D	V	L	Q	S	I	T	M	T

Actins attached with asterisks are deep-sea fish actins [20].

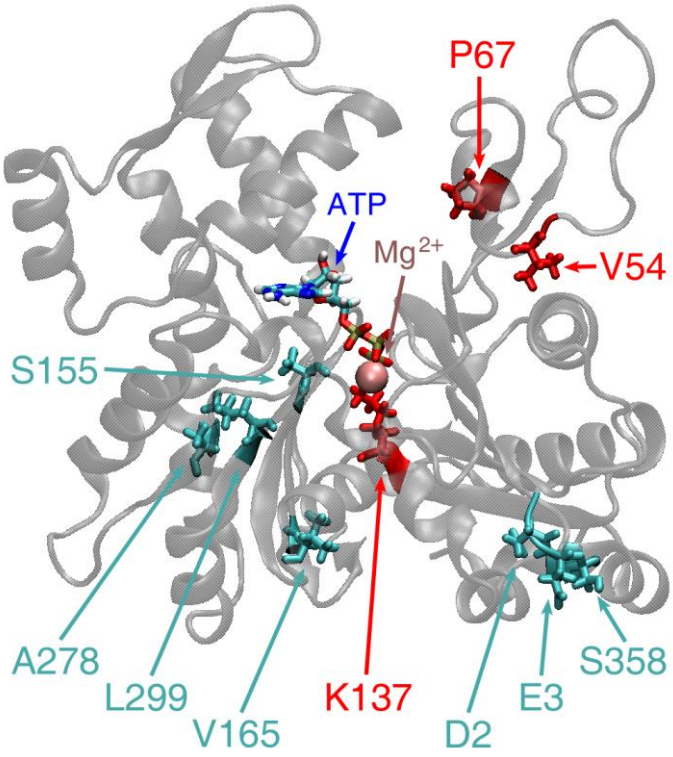

Figure 2. A snapshot of *C. yaquinae* actin 2b (600 bar) after 70-ns molecular dynamic simulations. The residues shown by red and cyan represent the specific substitutions in deep-sea fish actins and those of living in land or shallow water species, respectively. The figure was generated using VMD [15].

Molecular dynamics (MD) simulation is a powerful tool to investigate pressure effects on proteins. MD simulations were employed to investigate pressure denaturation, conformation changes, water penetration, or volume changes in wide range of pressure [26; 27; 28; 29]. In the case of ubiquitin, water penetrations were induced at around 3000 bar or greater and then denaturation was observed [26]. In addition, collapse of secondary structure and increase of the radius of gyration were studied by water-insertion method [29]. To examine the change of protein structures, solvent-accessible

surface area, and volume are often calculated using atom coordinates. Recently volume calculation method was improved [30]. NMR experiment and volume calculation with atomic coordinates showed that high pressure compressed protein decreasing only about 1-3 % of the volume [29]. Since most of globular proteins form highly packed structures in native state, volume change caused by high pressure is relatively small. To examine pressure effect, many small proteins such as ubiquitin [26], T4 lysozyme [27], or apomyoglobin [28] were investigated by MD simulations with all-atom models at high pressure. However, the detailed effects of pressure are not elucidated well.

To analyze the effects of amino acid substitutions, *in vivo* generation of actin mutants are necessary. However, it is well recognized that most of mutated actins cannot be expressed [25]. Therefore, almost of all experiments were carried out using actins purified from muscle fiber. On the other hand, it is easy to model mutated actins computationally such as deep-sea fish. This is why I chose MD simulations to investigate structures including in many mutated actins. Although the effects of these substitutions were observed in some experiments, the detailed mechanisms are still unclear in molecular level. The purpose of this study is to elucidate the mechanism of the pressure tolerance induced by substitutions.

2 Methods

2.1 Modeling of α-actin

First, I carried out structure modeling of *acrolepis*, rabbit, *armatus*, and *yaquinae* actins for MD simulations. I obtained coordinates of rabbit skeletal muscle α-actin with crystal waters, ATP, and Ca^{2+} from the crystal structure (PDB accession code 1WUA) [31]. The residues 42-50 at flexible DNase I binding loop, 1-4 at N-terminal residues, and 372-375 at C-terminal residues were missing in the crystal structure. The N-terminal residues 1-4 and residues 39-53 at DNase I binding loop were added using a crystal structure (PDB accession code 1ATN) [7] and the C-terminal residues 372-375 were complemented with a crystal structure (PDB accession code 1ESV) [32]. I added hydrogen atoms for the modeled residues using Visual Molecular Dynamics software package (VMD) [15].

Table 3. Details of the modeled rabbit α-actin amino acid sequence.

Residue	1-4	5-38	39-53	54-368	369-375
Resolution (Å)	2.80	1.45	2.80	1.45	2.00
PDB	1ATN	1WUA	1ATN	1WUA	1ESV

The PDB denotes PDB accession code of these residues.

Second, *acrolepis*, *armatus*, and *yaquinae* actins were modeled using the modeled rabbit actin. The Lys-137 substitution in *armatus* and *yaquinae* actins was optimized using evaluation of 81 Lys-137 rotamers. These Lys-137 rotamers were made as follows. Lysine has a long side-chain, which is rotated by five dihedral angles. The dihedral angles are called χ_1 to χ_5 from

near the C_α atom. Since the χ_5 angel at the end of side-chain is connected with symmetric amino group, I did not optimize the χ_5 angel rotamers. The side-chain carbon atoms are bound to two hydrogen atoms and two nonhydrogen atoms. Therefore, lysine side-chain rotamers can have low energies every about 120° rotations of each angle. To obtain the best rotamer for initial coordinates, I carried out structures modeling by lysine side-chain rotation every 120° and then made 81 rotamers with different low energies. These rotamers were minimized at the only Lys-137 total energy. Among the 81 rotamers, I chose a rotamer which have the third lowest energy and the longest distance between Ca^{2+} and Lys-137 side-chain nitrogen atom (Table 4. No.3). Since other substitution residues were short side-chain or on the surface of actin, other substitution rotamers were not optimized.

Table 4. Lys-137 side-chain rotamer energies and distances in different dihedral angles at the top eight low $E_{Lys\text{-}137}$.

No.	χ_1^{ini}	χ_2^{ini}	χ_3^{ini}	χ_4^{ini}	χ_1^{min}	χ_2^{min}	χ_3^{min}	χ_4^{min}	E_{total}	$E_{Lys\text{-}137}$	*d*
1	60	180	60	180	58.38	177.16	66.28	179.16	−5096.18	−35.47	3.18
2	60	180	180	180	60.37	174.61	−170.25	−172.89	−5089.78	−33.35	4.40
3	60	180	180	60	57.79	175.45	−171.69	56.45	−5077.66	−25.56	5.55
4	60	180	−60	180	62.58	−179.37	−51.41	−169.04	−5073.02	−19.19	2.11
5	60	180	60	−60	52.07	−176.81	71.09	−58.94	−5079.63	−17.73	3.79
6	60	180	−60	60	68.14	−178.73	−68.64	52.40	−5075.46	−15.28	2.61
7	−120	180	−60	180	−98.65	−161.69	−101.45	−177.13	−5072.70	−13.83	2.40
8	−120	180	60	180	−102.04	−162.09	40.46	−174.23	−5056.03	−6.44	1.10

These angles of χ^{ini} and χ^{min} denote angels of before minimization and after minimization, respectively. E_{total} and $E_{Lys\text{-}137}$ are the total energy of the whole protein and the only Lys-137 energy, respectively. The *d* is distance between Ca^{2+} and Lys-137 side-chain nitrogen atom. Units: χ, degree; E, kcal/mol; *d*, Å. Number three rotamer was chosen for the initial structure.

Ca^{2+} in the enzymatic pocket was replaced with Mg^{2+} due to fitting physiological conditions [16]. All of four actin models (i.e., *acrolepis*, rabbit, *armatus*, and *yaquinae* actin) were solvated with VMD plug-in *solvate*. The plug-in created boxes of water molecules and immersed the systems in water shells of 10 Å thickness. After solvation with water molecules, I carried out VMD plug-in *autoionize* to add 50 mM NaCl and then replaced Na^+ with K^+ using VMD plug-in *sod2pot*. Finally, *acrolepis*, rabbit, *armatus*, and *yaquinae* actin systems were solvated; 16733, 16734, 16734, and 16734 water molecules; 19, 19, 18, and 18 Cl^-, respectively, and 12 K^+ in common. The total system sizes of *acrolepis*, rabbit, *armatus*, and *yaquinae* actin were 56108, 56120, 56110, and 56111, respectively. Each actin has N-terminal acetyl-aspartate and 3-methylhistidine (3-MeH) on the residue 73. These modified residues were included in the crystal structures.

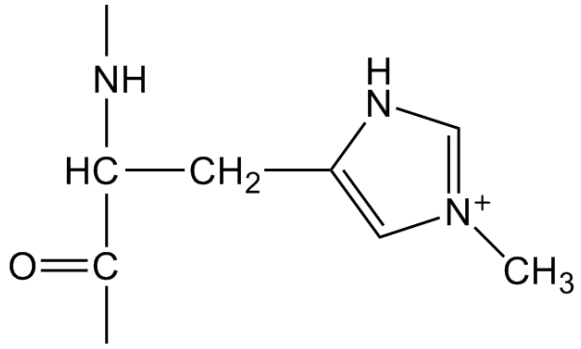

Figure 3. Constitutional formula of 3-MeH

2.2 Modification of parameter and topology files

I used the CHARMM22 parameter and topology files for MD simulations. They were modified to accommodate the SPC/E explicit water model, N-terminal acetyl-aspartate, and 3-MeH. CHARMM22 default water model

is TIP3P [33] and replaced with the SPC/E water model. The acetylated N-terminus patch was applied to the N-terminal aspartate acid. CHARMM22 parameter and topology files do not provide 3-MeH parameters and topology. Thus, charged 3-MeH parameters and topology were added using a doubly protonated histidine and a N-methylamide C-terminus patch in the standard CHARMM22 files [34].

2.3 Simulation procedure

The MD simulations were performed in the CHARMM22 force field [35] with the SPC/E water model [36] by using the NAMD software package [37]. The SPC/E water model density has been tested appropriately at 1 to 900 bar and 277 K. This test was carried out as follows. About $80 \times 80 \times 80$ Å^3 water boxes consisting of 16895 water molecules using rigid bonds and angles were run in an isobaric-isothermal ensemble (constant *NPT*) at 277 K for 2 ns after 1000 times minimizations of total energy. These simulations using SPC/E and TIP3P water model were performed at 1 bar and 100 to 900 bar every 100 bar independently. Last 1-ns trajectories were used for calculation of the density.

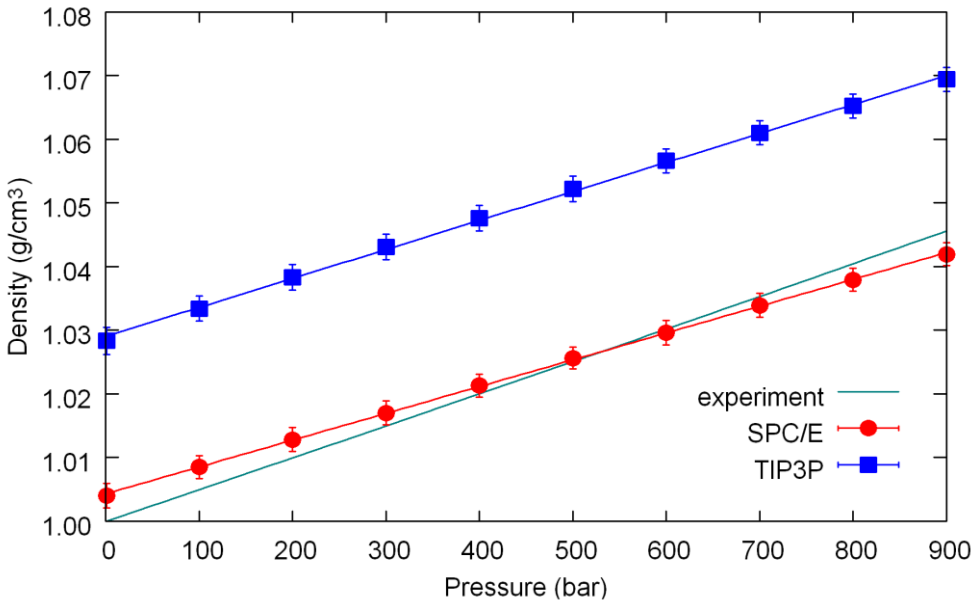

Figure 4. Water density changes induced by pressure. The Experimental value was derived from reference [38]. These error bars indicated the standard deviation.

Electrostatic potentials were calculated from the smooth particle mesh Ewald method [39], which was improved from the particle mesh Ewald sums [40] and the grid spacing of at least 1 Å was used. The van der Waals interactions were calculated using 12 Å cutoff and a smooth switching function. MD simulations were run with periodic boundary conditions in an isobaric-isothermal ensemble except for initial 2-ns simulations using a canonical ensemble (constant *NVT*). Constant temperature was maintained using Langevin dynamics of nonhydrogen atoms with a damping coefficient of 5 ps^{-1} and constant pressure was controlled with Langevin piston Nosé-Hoover barostat [41; 42] with an oscillation period of 100 fs and a decay time of 50 fs. All hydrogen bonds were rigid using the SHAKE algorithm [43] and the internal geometry of water molecule was rigid using the SETTLE

algorithm [44]. Simulations were carried out at 277 K and 1 or 600 bar except for initial 2-ns simulations. The integration time step of 2 fs was used and simulations were run for 70 ns; 40 ns equilibration and 30 ns samplings. The coordinates and energy data were stored every 0.5 and 0.1 ps, respectively.

After 3000 times minimizations of total energy, MD simulations were performed with fixed original protein atoms (not modeled atoms), Lys-137, ATP, and Mg^{2+} at the initial coordinates for 1 ns. Then I changed the fixes for harmonic constraints and performed simulations for 1 ns. The initial constraints using 1 kcal/mol gradually decreased by 0.1 kcal/mol every 0.1 ns. After simulations with constraints, rabbit actins and 32 same replicas making of *acrolepis* actin coordinate and velocity were carried out at 1 bar for 0.1 ns independently. I obtained two distinct states of Mg^{2+} coordination are considered: coordinated by four water molecules and ATP (*acrolepis*$_{Wat}$); coordinated by three water molecules, ATP, and a Gln-137 side-chain atom (*acrolepis*$_{Gln}$). Although rabbit actin also has Gln-137, it was not coordinated for Mg^{2+} using 32 rabbit actin replicas. On the other hands, I performed simulations with *armatus* and *yaquinae* actins at 1 bar for 0.1 ns without replicas due to the Q137K substitution. Five different structures (*acrolepis*$_{Wat}$, *acrolepis*$_{Gln}$, rabbit, *armatus*, and *yaquinae* actin) were run with two manners. The low pressure manner maintained pressure at 1 bar whereas the high pressure manner raised pressures gradually at 2 to 600 bar by 2 bar every 0.03 ns and then maintained the pressure at 600 bar.

2.4 Excluded volume and solvent-accessible surface area

Excluded volume (V_{ex}) and solvent-accessible surface area (SASA) calculated using CAVE software package [30]. The definition of SASA is a track of a probe center when the probe rolls around the whole protein surface. In addition, the space of the inside of the track is defined as V_{ex}. The probe radius was 1.4 Å and the atom radii were used with the van der Waals radii. This probe size denotes an oxygen atom of the water molecule in solution. These van der Waals radii were distinguished from the bonds: tetrahedral carbon, tetrahedral nitrogen, and sulfur with hydrogens were 2.0 Å; trigonal carbon and trigonal NH were 1.7 Å; trigonal CH, CH_2, and sulfur were 1.85 Å; trigonal NH_2 was 1.8 Å; oxygen was 1.4 Å [45]. Input coordinates of the PDB file format from trajectories were generated using VMD [15].

2.5 Moment of inertia

Moment of inertia (MOI) represents the form and spread of structures. In particularly, MOI is associated with the motion of rotations. In other words, large external forces are needed when structures with large MOI begin to rotate. Since MOI depends on rotational axes, it is important to set the axes. I chose principal axes of each structure to analyze because protein has anisotropic structures and symmetric axes do not exist. These principal axes can be calculated with the MOI tensor. This tensor is defined as equation 1:

$$\mathbf{I} = \begin{pmatrix} I_{xx} & I_{xy} & I_{xz} \\ I_{yx} & I_{yy} & I_{yz} \\ I_{zx} & I_{zy} & I_{zz} \end{pmatrix}$$
$$= \begin{pmatrix} \sum_i^N m_i(y_i^2 + z_i^2) & -\sum_i^N m_i x_i y_i & -\sum_i^N m_i x_i z_i \\ -\sum_i^N m_i y_i x_i & \sum_i^N m_i(z_i^2 + x_i^2) & -\sum_i^N m_i y_i z_i \\ -\sum_i^N m_i z_i x_i & -\sum_i^N m_i z_i y_i & \sum_i^N m_i(x_i^2 + y_i^2) \end{pmatrix}, \quad (1)$$

where N is the number of atoms, m_i is the mass of ith atom, and Cartesian coordinates are positions of these atoms. Since the MOI tensor is a real and symmetric matrix, it can be diagonalized. After diagonalization, I obtained eigenvalues ($I_1 > I_2 > I_3$) called principal moment of inertia (PMOI) and axes consisting of eigenvectors ($\boldsymbol{e_1}$, $\boldsymbol{e_2}$, and $\boldsymbol{e_3}$) called principal axis of inertia (PAOI). Each PMOI represented the MOI for each PAOI. Although protein has complex atom distribution, PMOI can measure the form and spread of the structures.

2.6 Coordination number

Coordination number (CN) for a cation is defined as the number of atoms within the distance between the cation atom and an oxygen atom is less than a criterion. The criterion for Mg^{2+} was set as 2.3 Å based on a radial distribution function (RDF) for Mg^{2+}. I performed simulations to decide the criterion as follows. Mg^{2+} was immersed in water shells of 40 Å thickness using VMD plug-in *solvate* and added two Cl^-. The MD simulations were run with periodic boundary conditions in an isobaric-isothermal ensemble at 277

K and 1 bar. After 3000 times minimizations of total energy, MD simulations were performed for 8 ns. The last 1-ns trajectories were used to calculate the RDF and the number of total water molecules for Mg^{2+}. Oxygen atoms represented each water molecule position.

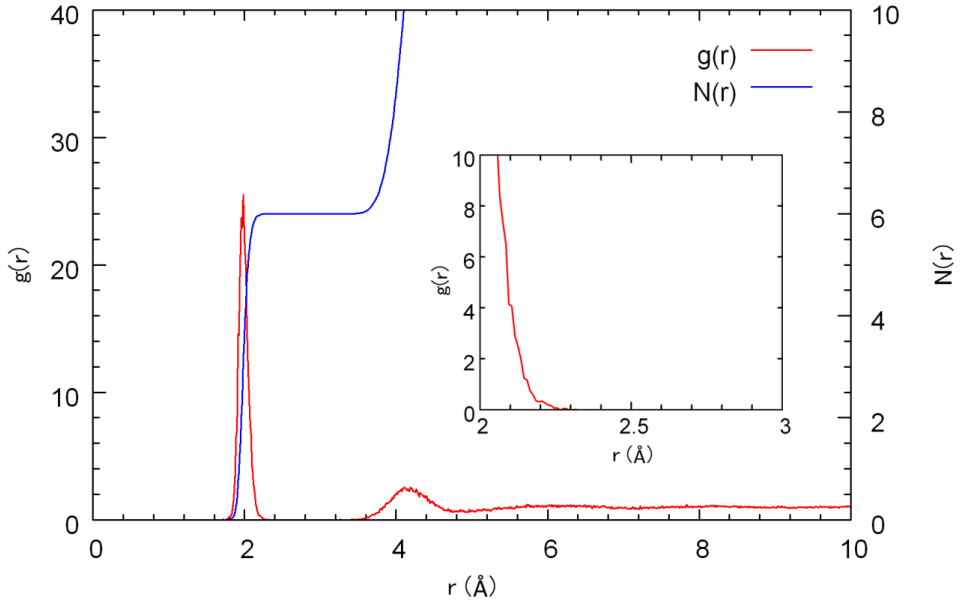

Figure 5. The RDF and the number of total water molecules for Mg^{2+} in solution, where r is the distance between Mg^{2+} and an oxygen atom, g(r) is the RDF, and N(r) is the number of total water molecules within r.

The first peak of the RDF is about 2 Å, and disappeared at about 2.3 Å. Therefore, I defined the criterion as 2.3 Å for all simulations. In addition, the CN was about six and corresponded to the lowest free-energy of Mg^{2+} in aqueous solution [46].

2.7 Salt bridge

Salt bridge is one of the interactions between charged atoms in side-chain or ligand atoms. The salt bridge is defined as electrostatic interaction between positive charged and negative charged atoms within the criterion of a distance. The distance between a charged oxygen atom and a charged nitrogen atom was set as 3.2 Å [15].

3 Results and Discussion

3.1 Excluded volume and solvent-accessible surface area

V_{ex} and SASA were calculated using trajectories every 0.01 ns to examine structure changes induced by high pressure. When protein denatured in high pressure, the conformation was changed and SASA highly increased [28]. However, SASA in all species increased by 2 % at most and denaturation did not occur. Thus, each structure was not collapsed at 600 bar by MD simulations. Some previous study showed high pressure induced volume decrease [47]. The result had a same tendency except for *acrolepis*$_{Gln}$ actin. On the other hands, the V_{ex} difference in *acrolepis*$_{Gln}$ actin was small positive value. Although *acrolepis*$_{Wat}$ and *acrolepis*$_{Gln}$ actins had a same amino acid sequence, the V_{ex} difference was different values. Therefore, coordinated atoms can highly affect their structures. In other words, Q137K substitution in deep-sea fish actins is expected to contribute to the pressure tolerance. The tendency of the V_{ex} changes induced by high pressures decreased less than 1 % whereas SASA increased slightly. According to the result of SASA, all actin structures were changed at high pressure. Although SASA difference in each deep-sea fish actin was a slight low value, these differences were smaller in relation to its standard deviation. Therefore, the meaningful differences in V_{ex} and SASA were not observed.

Table 5. Comparison of V_{ex} and SASA in different species.

Actin	$V_{ex,1bar}$	$V_{ex,600bar}$	$SASA_{1bar}$	$SASA_{600bar}$	ΔV_{ex}	$\Delta SASA$
acrolepis$_{Wat}$	73966 ± 230	73801 ± 292	18334 ± 165	18513 ± 304	−165	179
acrolepis$_{Gln}$	74107 ± 236	74144 ± 241	18448 ± 180	18798 ± 191	36	350
Rabbit	73769 ± 206	73734 ± 227	18112 ± 145	18427 ± 184	−35	315
armatus	73774 ± 222	73494 ± 218	18200 ± 159	18293 ± 153	−280	93
yaquinae	74129 ± 216	73905 ± 219	18507 ± 195	18531 ± 216	−223	23

Subscripts of V_{ex} and SASA denote simulation pressure. The ΔV_{ex} and $\Delta SASA$ were defined as $\Delta V_{ex}=V_{ex,600bar}-V_{ex,1bar}$ and $\Delta SASA=SASA_{600bar}-SASA_{1bar}$, respectively. These V_{ex} and SASA were calculated using 40-70ns trajectories. Units: V_{ex}, $Å^3$; SASA, $Å^2$.

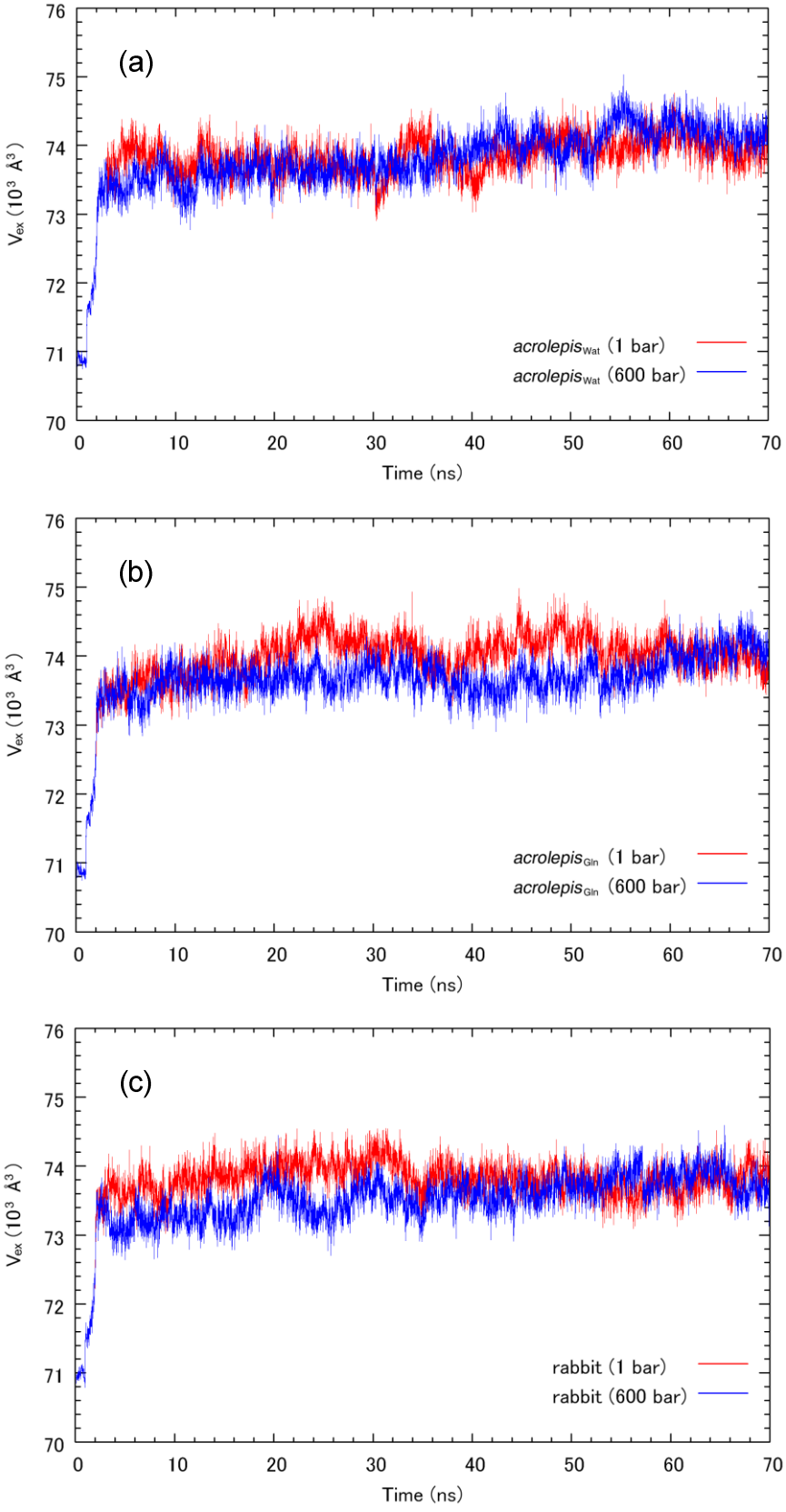
(a)
V_{ex} (10^3 Å^3)
Time (ns)
acrolepis$_{Wat}$ (1 bar)
acrolepis$_{Wat}$ (600 bar)
(b)
V_{ex} (10^3 Å^3)
Time (ns)
acrolepis$_{Gln}$ (1 bar)
acrolepis$_{Gln}$ (600 bar)
(c)
V_{ex} (10^3 Å^3)
Time (ns)
rabbit (1 bar)
rabbit (600 bar)

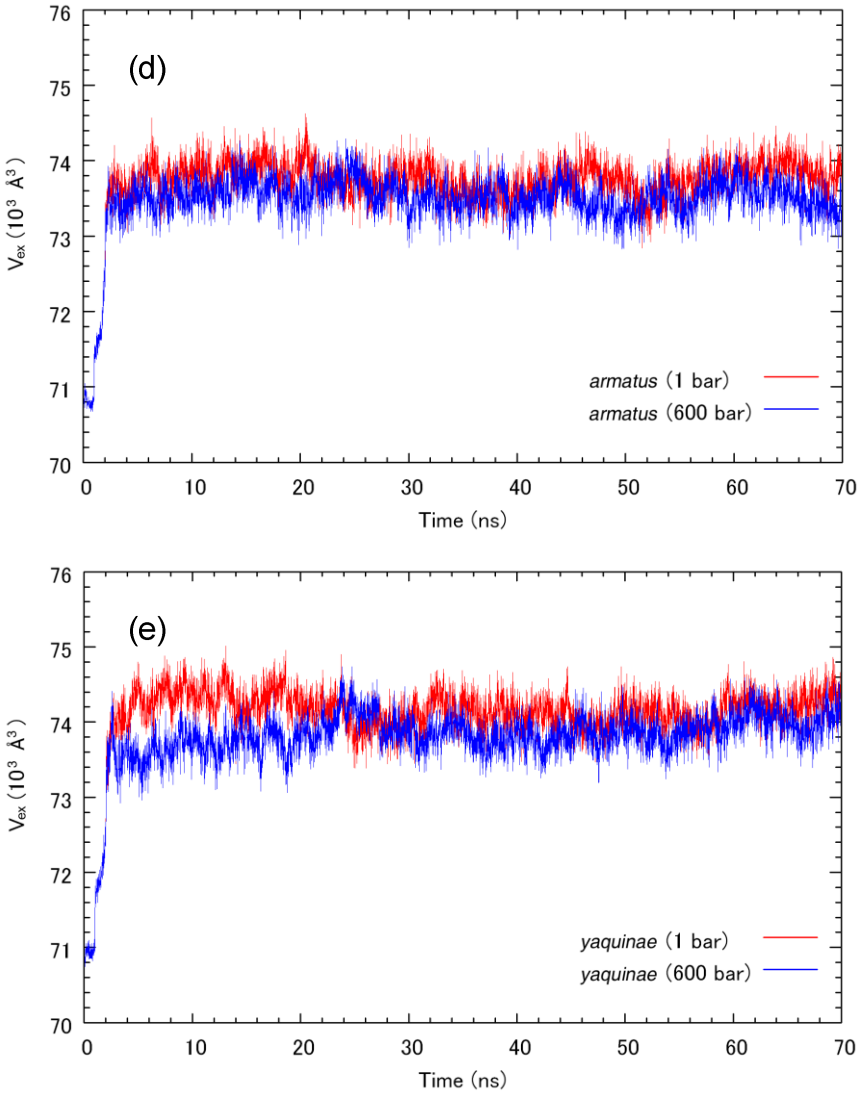

Figure 6. V_{ex} changes using only actin atom coordinates in different species at 1 or 600 bar. Each value was calculated by CAVE software package [30].

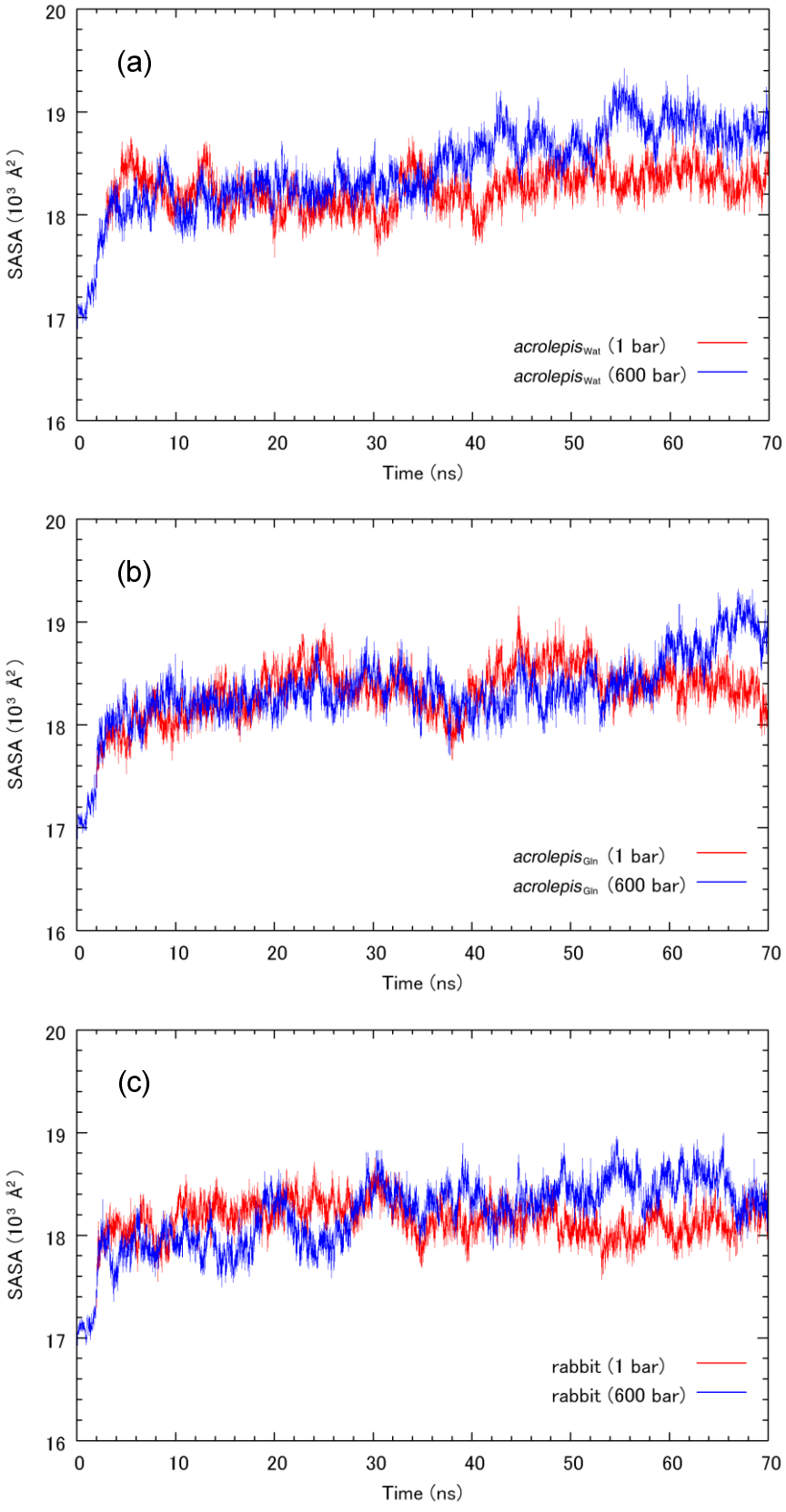
(a)
SASA (10³ Å²)
Time (ns)
acrolepis_Wat (1 bar)
acrolepis_Wat (600 bar)
(b)
SASA (10³ Å²)
Time (ns)
acrolepis_Gln (1 bar)
acrolepis_Gln (600 bar)
(c)
SASA (10³ Å²)
Time (ns)
rabbit (1 bar)
rabbit (600 bar)

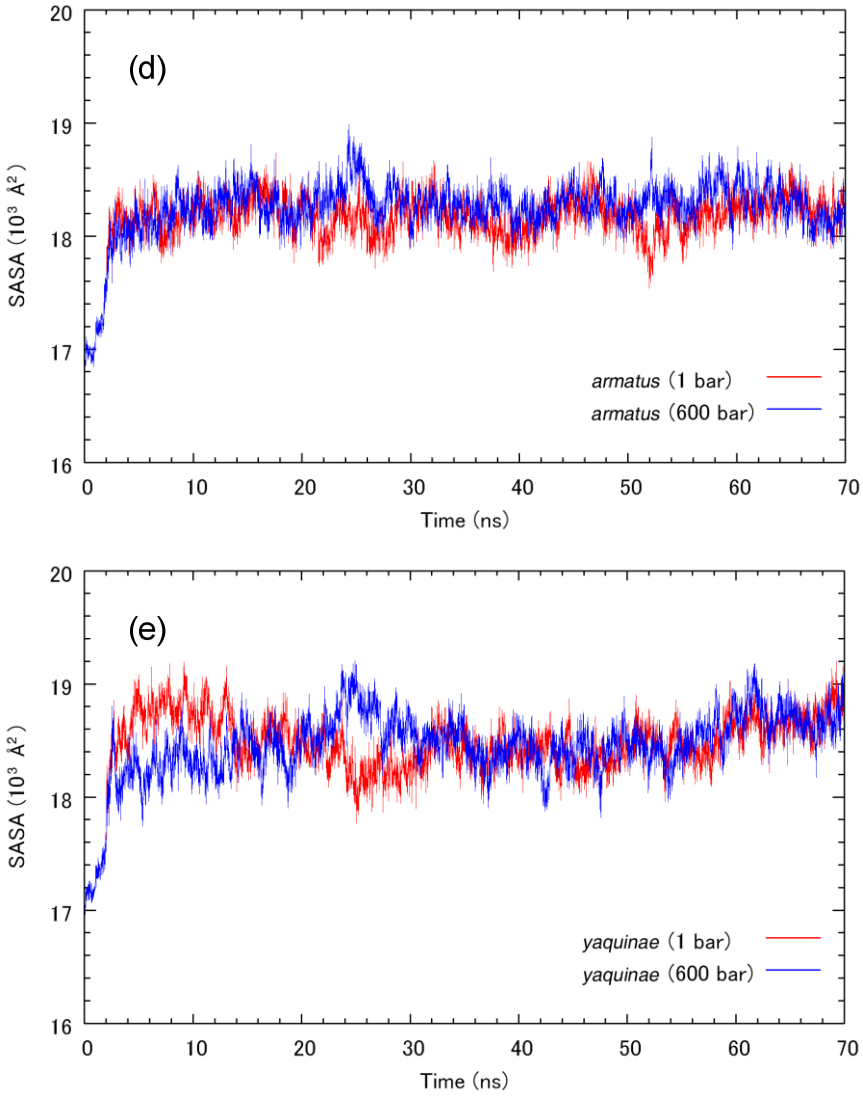

Figure 7. SASA changes using only actin atom coordinates in different species at 1 or 600 bar. Each value was calculated by CAVE software package [30].

3.2 Principal moment of inertia

I calculated each PMOI using only actin atom coordinates except for hydrogen atoms to investigate the structure changes, especially anisotropic structures. Although the result of V_{ex} and SASA showed the tendency of structure changes, these values were not considered about anisotropic changes. Each actin has a similar disciform structure (Figure 8). Since actin was a disciform structure, the center of gravity was almost corresponded to the active site. In addition, the 1st PAOI penetrated the active site and all subdomains were expanded around the axis. Since subdomain 2 is a small subdomain, the 2nd PAOI axis seems to penetrate subdomain 2 and 3. Actins living in land or shallow water were affected by high pressure and each PMOI increased. Among three axes, the most notable difference was seen in 1st PMOI. In other words, actin form was changed into thinner and more spread structure. Since only *acrolepis*$_{Wat}$ actin decreased 1st PMOI, it meant that *acrolepis*$_{Wat}$ actin was also changed. These conformational changes may induce miss matching of the actin-actin interaction in filament and inhibition of elongation at high pressure. Therefore, deep-sea fish actins are suggested to maintain their structures at high pressure whereas actins living in land or shallow water would be changed into compressed structures by high pressure.

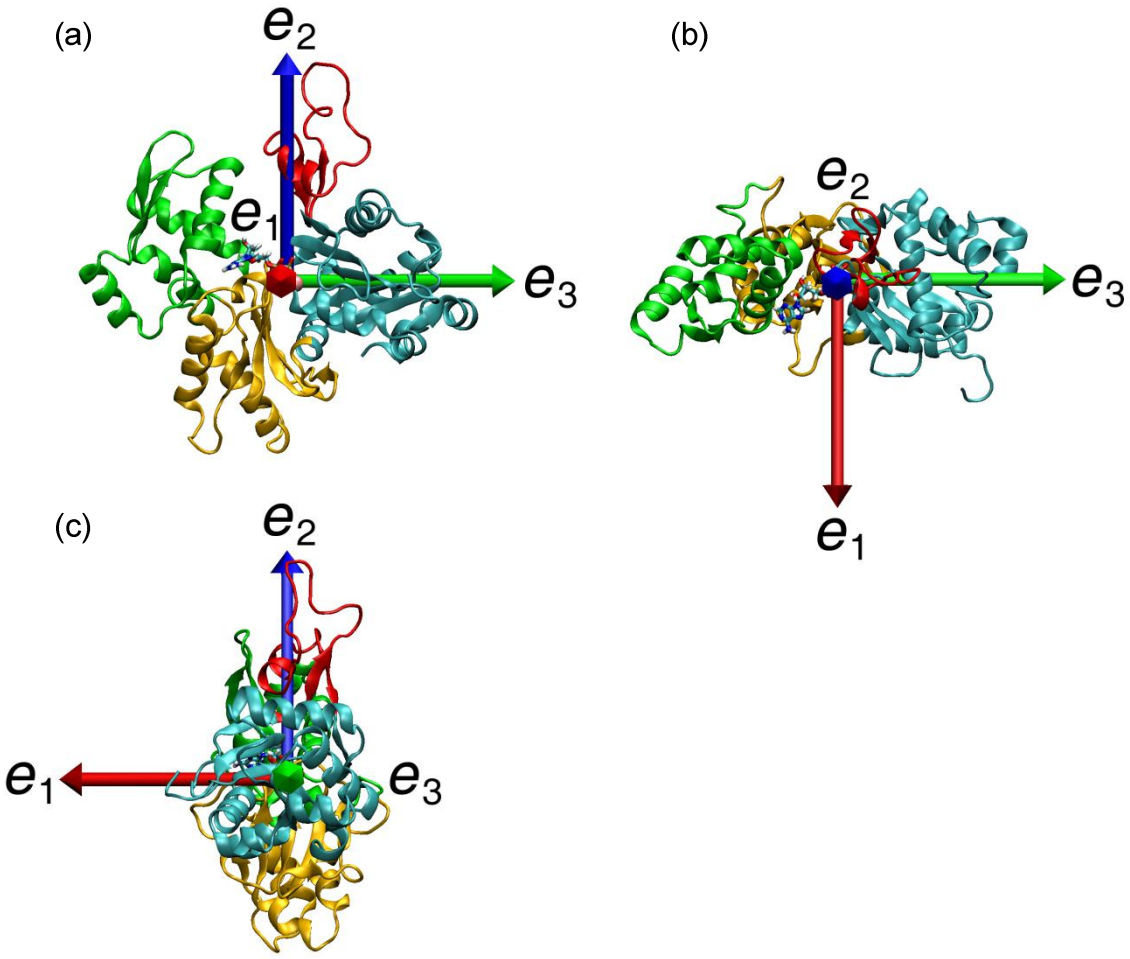

Figure 8. A snapshot of *yaquinae* actin (600 bar) after 70-ns MD simulations. These red e_1, blue e_2, and green e_3 arrows indicate vectors of 1st, 2nd, and 3rd PAOI, respectively. The figures were generated using VMD [15].

Table 6. Each PMOI of heavy atoms in different species.

Actin	$PMOI_{1bar}^{1st}$	$PMOI_{1bar}^{2nd}$	$PMOI_{1bar}^{3rd}$	$PMOI_{600bar}^{1st}$	$PMOI_{600bar}^{2nd}$	$PMOI_{600bar}^{3rd}$	$\Delta PMOI^{1st}$	$\Delta PMOI^{2nd}$	$\Delta PMOI^{3rd}$
acrolepis$_{Wat}$	16.84±0.13	12.14±0.10	9.40±0.09	16.46±0.16	11.92±0.20	9.41±0.09	−0.38	−0.23	0.02
acrolepis$_{Gln}$	16.78±0.11	12.06±0.11	9.36±0.06	17.09±0.15	12.43±0.18	9.42±0.10	0.32	0.37	0.06
Rabbit	16.96±0.11	12.10±0.13	9.36±0.13	17.23±0.13	12.45±0.13	9.30±0.08	0.27	0.35	−0.06
armatus	16.80±0.14	12.18±0.12	9.20±0.07	16.98±0.13	12.27±0.18	9.25±0.08	0.18	0.08	0.05
yaquinae	16.74±0.11	12.06±0.10	9.29±0.10	16.91±0.11	12.09±0.12	9.31±0.06	0.16	0.03	0.01

Upper and lower subscripts of PMOI denote the order of PMOI and pressure, respectively. The ΔPMOI was defined as $\Delta PMOI = PMOI_{600bar} - PMOI_{1bar}$. Each PMOI was calculated using 40-70ns trajectories. Unit: PMOI, 10^6·g/mol·Å^2.

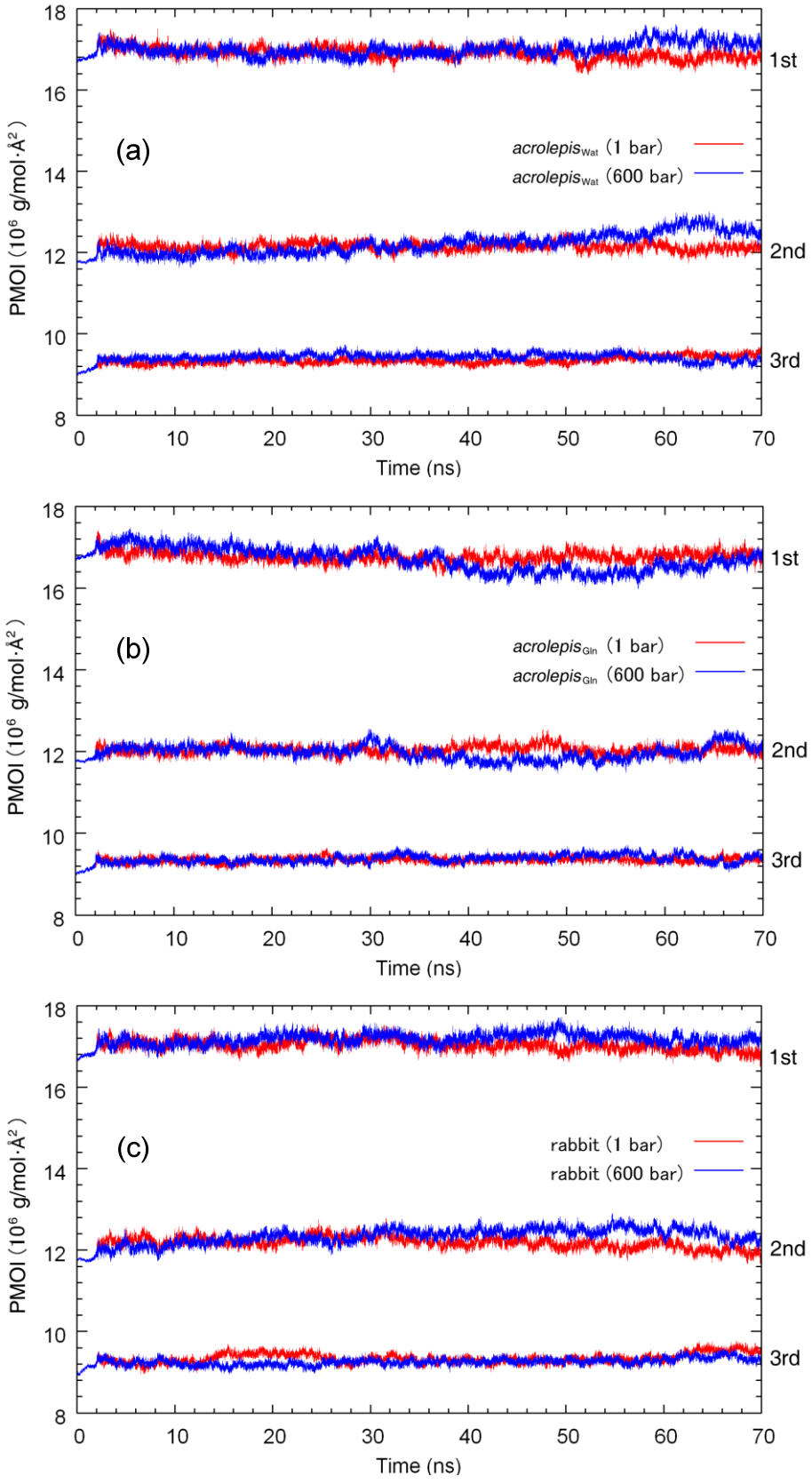
(a)
acrolepis$_{Wat}$ (1 bar)
acrolepis$_{Wat}$ (600 bar)
1st
2nd
3rd
PMOI (10^6 g/mol·Å^2)
Time (ns)
(b)
acrolepis$_{Gln}$ (1 bar)
acrolepis$_{Gln}$ (600 bar)
1st
2nd
3rd
PMOI (10^6 g/mol·Å^2)
Time (ns)
(c)
rabbit (1 bar)
rabbit (600 bar)
1st
2nd
3rd
PMOI (10^6 g/mol·Å^2)
Time (ns)

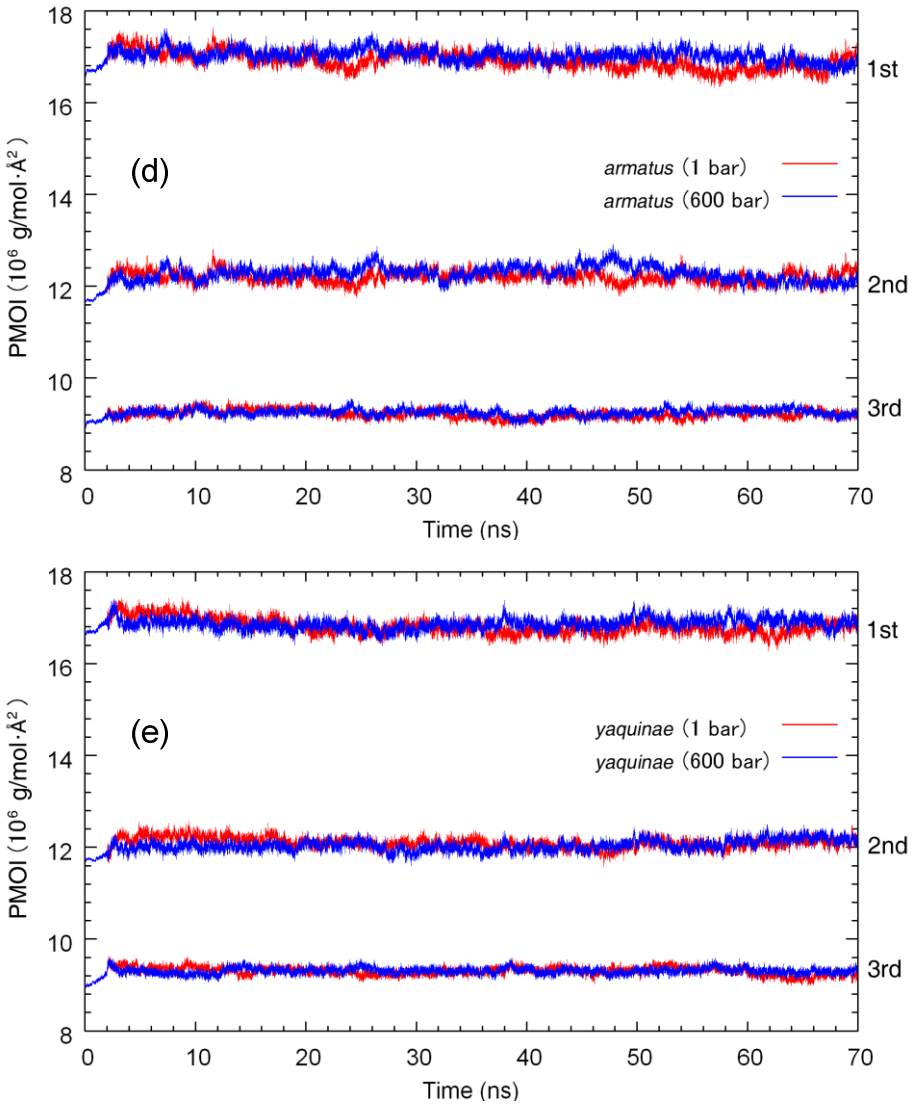

Figure 9. Each PMOI of heavy atoms in different species at 1 or 600 bar.

3.3 Distances and the dihedral angle between subdomains

Actin is consisted of four subdomains which can twist like a propeller. The dihedral angle θ and the distances d_{sub} between subdomains were calculated to examine the relationship of subdomain positions. These distances between subdomains were calculated as a distance between the center of gravity in one subdomain and another (Figure 10). Each distance between subdomains was a similar value compared to actins at 1 and 600 bar. Previous study showed that G-actin had a low energy when the dihedral angle equaled about −20° [8]. The result of dihedral angles at 1 bar showed only *yaquinae* actin had the difference of θ was a positive value. Moreover, the dihedral angle of *yaquinae* actin at 600 bar twisted only about −13° whereas other species twisted by about −20 to −24°. In other words, *yaquinae* actin at 600 bar had more flat form than other species. Although *yaquinae* actin is suggested to elongate the filament stably at high pressure, *armatus* actin, which is also deep-sea fish, had the dihedral angle twisted by about −22° at 600 bar. Therefore, there is not notable value which both *yaquinae* and *armatus* actins have in common.

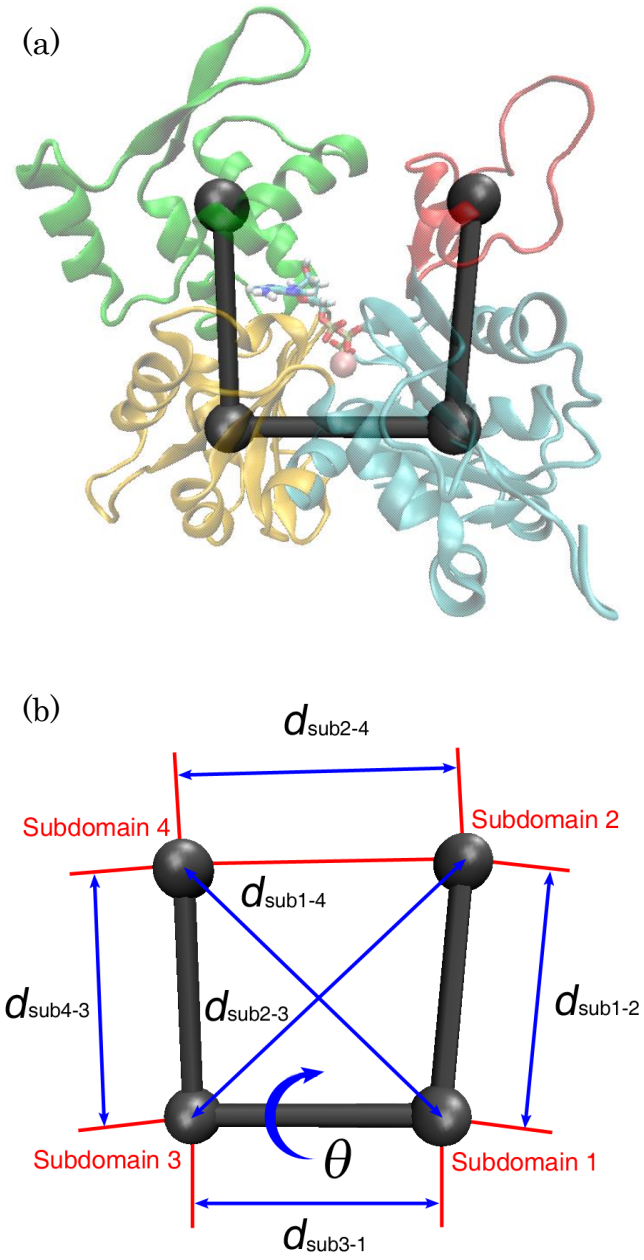

Figure 10. The definitions of distance d_{sub} and dihedral angle θ between subdomains. (a) A snap shot of *yaquinae* actin (600 bar) after 70-ns MD simulations. Gray spheres and bonds indicate the center of gravity in each subdomain and bonds between the centers of gravity, respectively. (b) Gray spheres and bonds are same as in (a).

Table 7. Distances between subdomains in different species.

(a)

Actin	Pressure	$d_{sub1\text{-}2}$	$d_{sub2\text{-}4}$	$d_{sub4\text{-}3}$	$d_{sub3\text{-}1}$	$d_{sub1\text{-}4}$	$d_{sub2\text{-}3}$
acrolepis$_{Wat}$	1	25.80±0.26	28.55±0.77	25.17±0.28	25.92±0.19	35.69±0.22	37.81±0.34
acrolepis$_{Gln}$	1	26.00±0.29	29.58±0.35	25.19±0.17	25.84±0.20	35.71±0.25	38.54±0.25
Rabbit	1	25.02±0.42	31.40±0.59	24.90±0.15	25.68±0.22	35.34±0.26	39.56±0.27
armatus	1	24.69±0.31	30.03±0.67	25.03±0.20	25.70±0.17	35.95±0.30	37.97±0.32
yaquinae	1	25.29±0.35	29.85±0.49	24.78±0.27	25.70±0.24	35.47±0.21	38.43±0.34
acrolepis$_{Wat}$	600	25.34±0.53	30.71±0.95	24.76±0.14	25.33±0.19	34.80±0.24	38.85±0.42
acrolepis$_{Gln}$	600	25.93±0.43	31.27±0.74	24.90±0.15	26.00±0.22	35.92±0.30	39.14±0.30
Rabbit	600	25.35±0.36	30.98±0.76	25.01±0.15	26.32±0.26	35.96±0.23	39.18±0.36
armatus	600	24.68±0.38	33.08±0.85	24.98±0.18	25.56±0.16	35.58±0.24	39.89±0.40
yaquinae	600	25.56±0.27	30.53±0.40	24.74±0.15	25.50±0.21	35.81±0.25	38.86±0.34

(b)

Actin	$\Delta d_{\mathrm{sub1\text{-}2}}$	$\Delta d_{\mathrm{sub2\text{-}4}}$	$\Delta d_{\mathrm{sub4\text{-}3}}$	$\Delta d_{\mathrm{sub3\text{-}1}}$	$\Delta d_{\mathrm{sub1\text{-}4}}$	$\Delta d_{\mathrm{sub2\text{-}3}}$
acrolepis$_{\mathrm{Wat}}$	−0.46	2.17	−0.41	−0.59	−0.89	1.04
acrolepis$_{\mathrm{Gln}}$	−0.08	1.68	−0.28	0.17	0.21	0.60
Rabbit	0.33	−0.42	0.11	0.63	0.62	−0.37
armatus	−0.01	3.04	−0.05	−0.13	−0.36	1.92
yaquinae	0.27	0.68	−0.04	−0.20	0.34	0.43

(a) Distances between subdomains at 1 or 600 bar. Subscripts of d_{sub} denote subdomain numbers. The d_{sub} was calculated using 40-70ns trajectories. Units: pressure, bar; d_{sub}, Å. (b) The difference of $d_{\mathrm{sub.}}$ The Δd_{sub} was defined as $\Delta d_{\mathrm{sub}} = d_{\mathrm{sub}}(600\mathrm{bar}) - d_{\mathrm{sub}}(1\mathrm{bar})$.

Table 8. Dihedral angles between subdomains in different species.

Actin	$\theta_{1\text{bar}}$	$\theta_{600\text{bar}}$	$\Delta\theta$
acrolepis$_{\text{Wat}}$	−20.18 ± 3.04	−23.96 ± 2.03	−3.78
acrolepis$_{\text{Gln}}$	−20.94 ± 1.78	−24.06 ± 2.21	−3.13
Rabbit	−16.99 ± 1.93	−20.33 ± 3.37	−3.35
armatus	−16.63 ± 2.07	−22.41 ± 3.40	−5.77
yaquinae	−17.94 ± 1.83	−13.52 ± 2.10	4.42

Subscripts of θ denote simulation pressure. The $\Delta\theta$ was defined as $\Delta\theta = \theta_{600\text{bar}} - \theta_{1\text{bar}}$. The θ was calculated using 40-70ns trajectories. Unit: θ, degree.

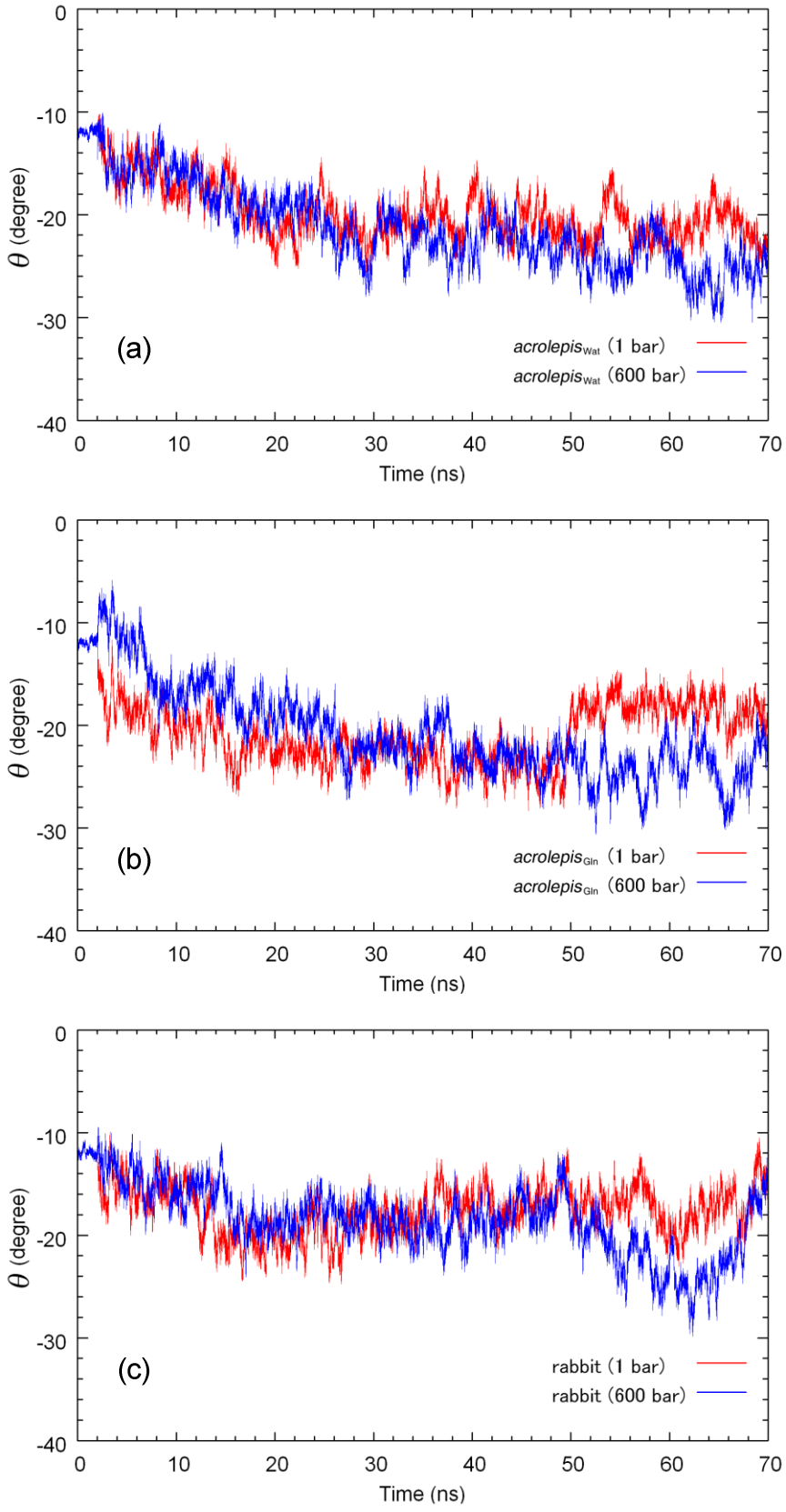
0
-10
-20
-30
-40
θ (degree)
0
10
20
30
40
50
60
70
Time (ns)
(a)
acrolepis$_{Wat}$ (1 bar)
acrolepis$_{Wat}$ (600 bar)
(b)
acrolepis$_{Gln}$ (1 bar)
acrolepis$_{Gln}$ (600 bar)
(c)
rabbit (1 bar)
rabbit (600 bar)

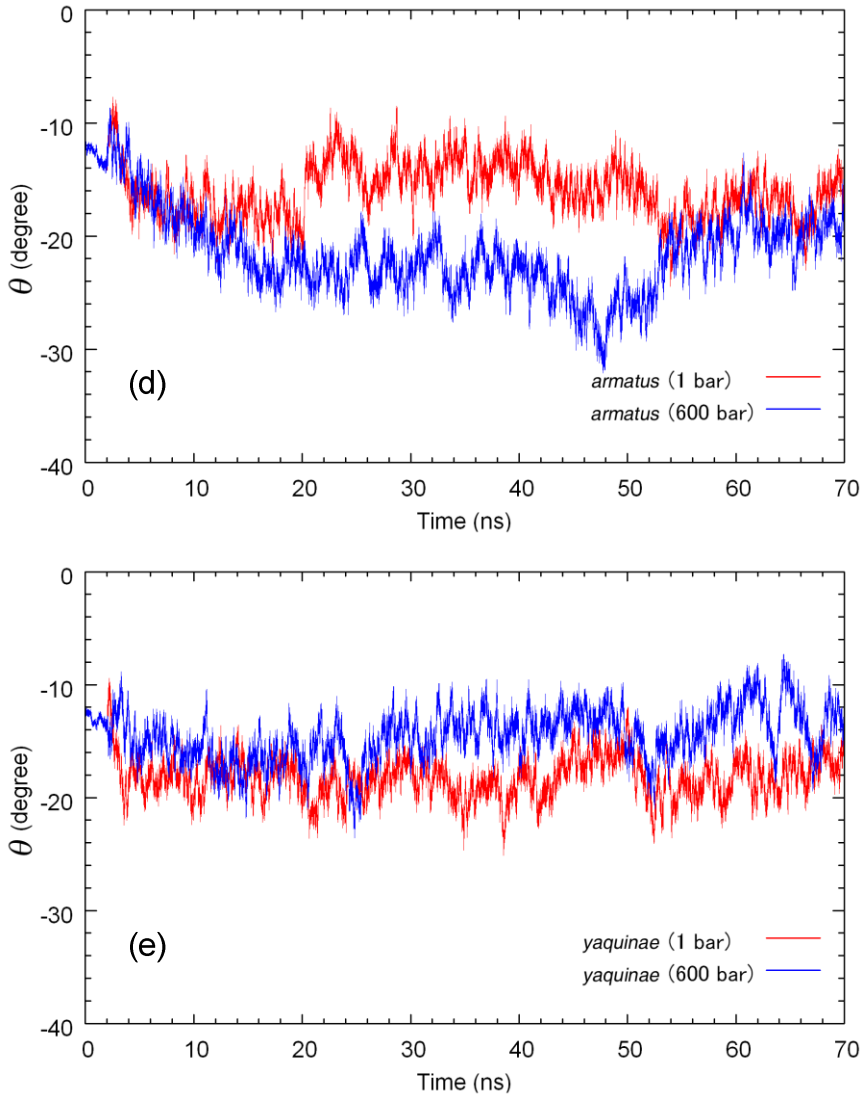

Figure 11. Dihedral angles between subdomains in different species at 1 or 600 bar.

3.4 Coordination number for Mg^{2+}

CN for Mg^{2+} at the active site was calculated to analyze effects of the substitutions. During all MD simulations, Mg^{2+} existed in the active site and oxygen atoms were coordinated stably. Although high pressure induced the structure changes, these coordinated atoms were not changed for 40-70 ns simulations. Only *acrolepis*$_{Gln}$ actin had a side-chain coordinated to Mg^{2+} and the coordinated atom maintained holding Mg^{2+} during the 40-70 ns simulations. The CN was about six in all species at both 1 and 600 bar although coordinated atoms were different. Previous study showed that Mg^{2+} can be coordinated by six water molecules stably [46]. In addition, four water molecules and two oxygen atoms included in ATP were also coordinated to Mg^{2+}. These two oxygen atoms called β- and γ-side oxygen were same atom positions in crystal structures [31].

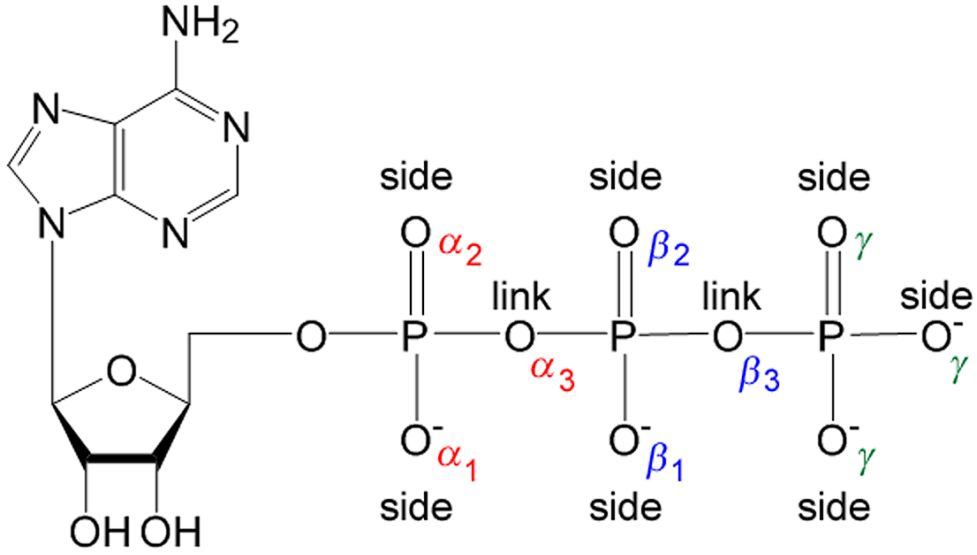

Figure 12. Constitutional formula of ATP.

In active site, side-chain atoms of residue 137 were different directions. Actins living in land or shallow water had Gln-137 whose side-chain was directed to Lys-18 side-chain atoms. On the other hand, deep-sea fish actins had Lys-137 whose side-chain was directed to opposite side for Gln-137. Therefore, deep-sea fish actins had different conformation at active site for other species. Compared to *acrolepis*$_{\mathrm{Wat}}$ and *acrolepis*$_{\mathrm{Gln}}$ actins, Gln-137 side-chain atoms, especially the end of side-chain, were different directions. Thus, *acrolepis*$_{\mathrm{Wat}}$ and *acrolepis*$_{\mathrm{Gln}}$ actins would behave as different actins. Previous study showed that high pressure induced increase of the dissociating rate for ATP and a divalent cation [20]. However, the CN was not changed and ligand atoms did not move at the active site. In addition, replacement of coordinated atoms did not occur although water molecules vibrated in simulations. Thus, the energy barrier in conformational changes between actin binding ligands and releasing ligands would be high and the transition rarely occurs in simulations. Since the ligands were bound at the active site tightly, conformational changes releasing ligands may need long time simulations or assists using external potentials.

(a)

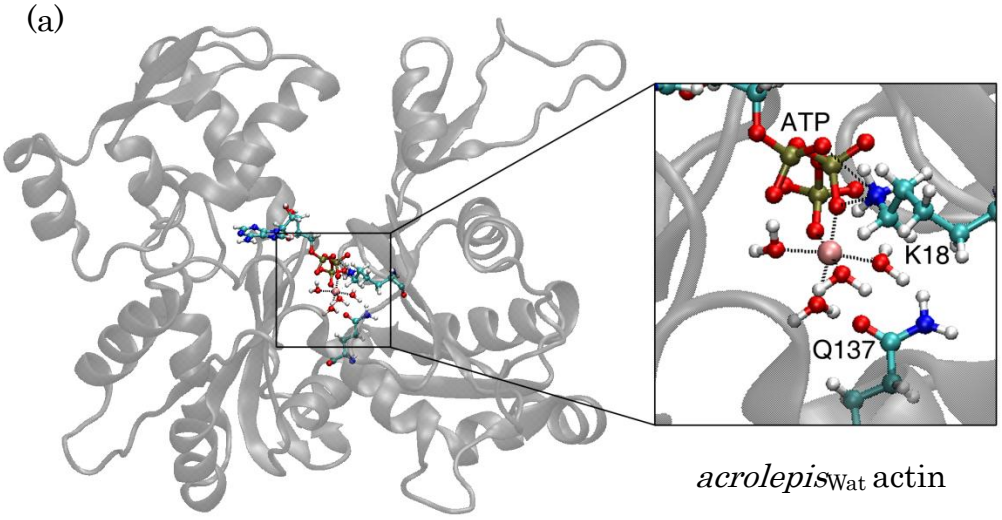

acrolepis$_{\mathrm{Wat}}$ actin

(b)

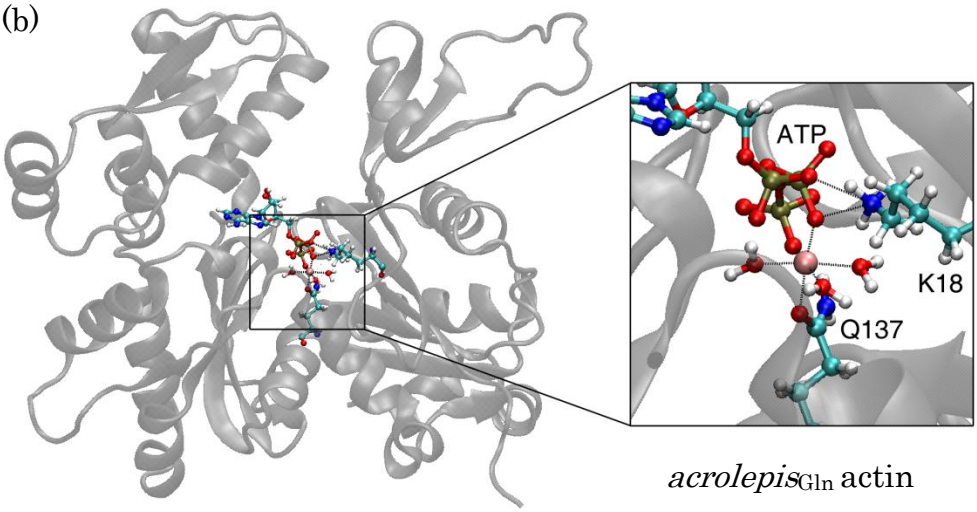

acrolepis$_{\mathrm{Gln}}$ actin

(c)

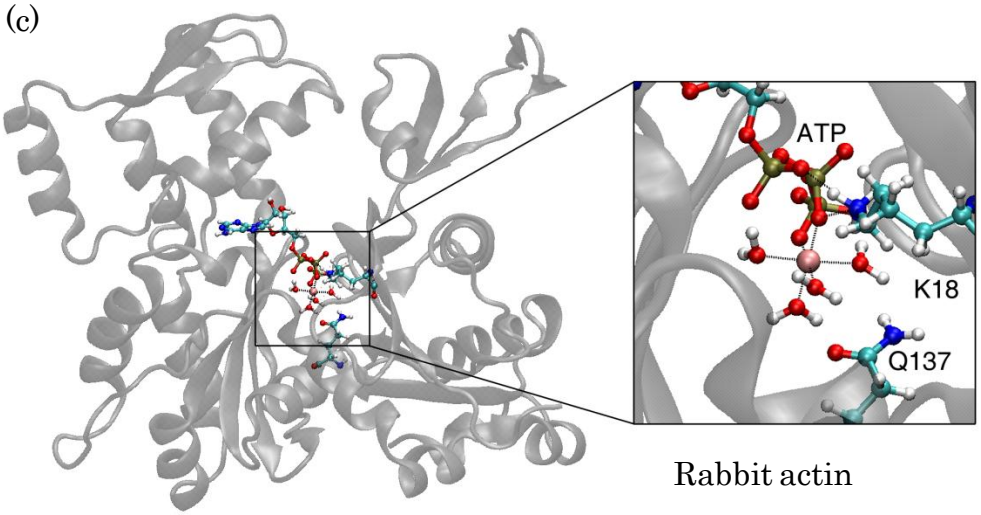

Rabbit actin

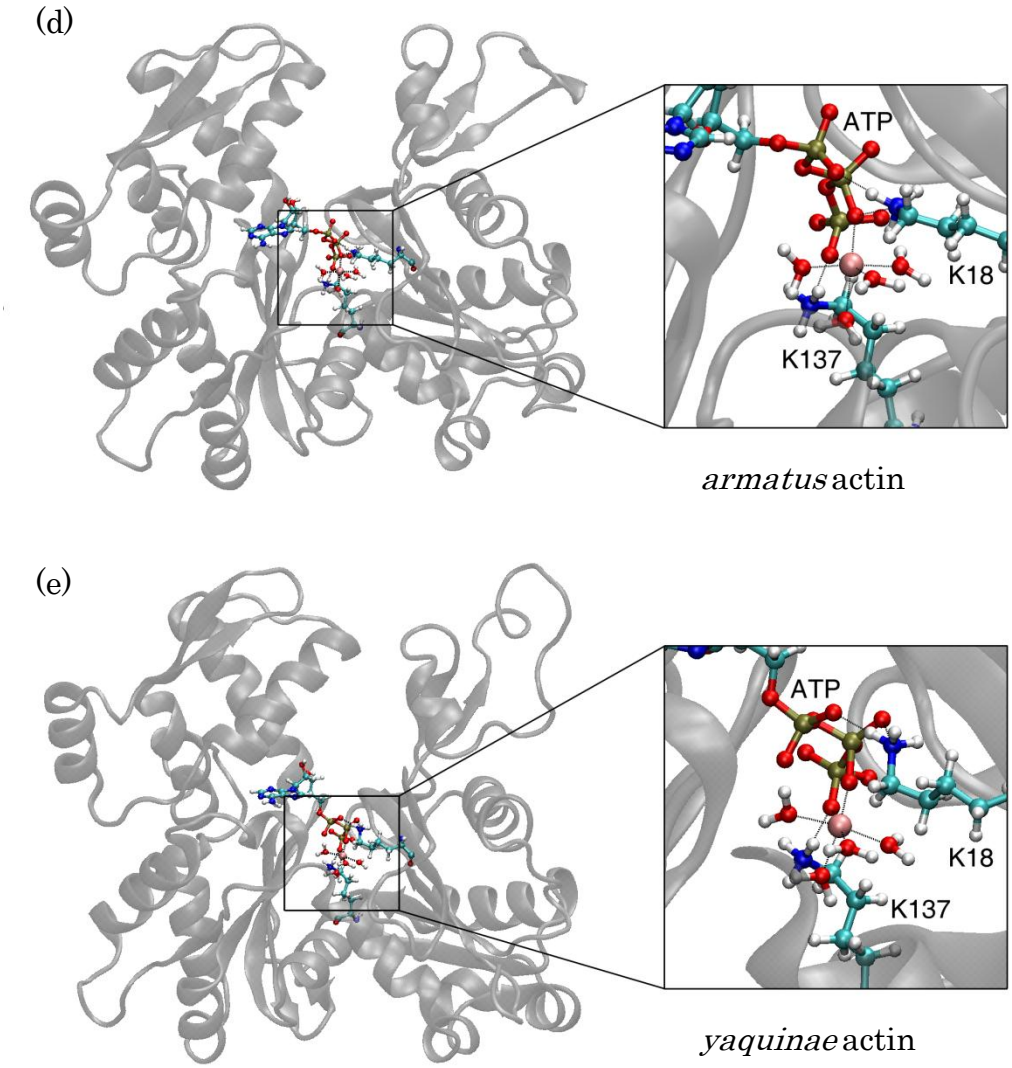

Figure 13. Coordinated atoms for Mg^{2+} at the active site. A pink sphere indicates Mg^{2+}. Only coordinated water molecules are shown. A broken line denotes a bond between Mg^{2+} and coordinated water molecules or salt bridge atoms. Each snapshot is actin (600 bar) after 70-ns MD simulations. These figures were generated using VMD [15].

Table 9. CN for Mg^{2+} at active site in different species.

Actin	CN_{1bar}	CN_{600bar}	ΔCN
acrolepis$_{Wat}$	5.99 ± 0.10	6.00 ± 0.07	0.01
acrolepis$_{Gln}$	6.00 ± 0.07	5.99 ± 0.09	−0.01
Rabbit	6.00 ± 0.07	5.99 ± 0.08	−0.01
armatus	5.99 ± 0.09	5.98 ± 0.14	−0.01
yaquinae	6.00 ± 0.07	5.99 ± 0.08	−0.01

Subscripts of CN denote simulation pressure. The ΔCN was defined as $\Delta CN = CN_{600bar} - CN_{1bar}$. The CN was calculated using 40-70ns trajectories.

3.5 Salt bridge analysis

To investigate the interactions between residues, I counted the number of salt bridges. The number of total salt bridges (NSB) was different in species and pressures. The difference of NSB (ΔNSB) in *acrolepis*$_{\mathrm{Wat}}$ was the lowest value. On the other hand, *acrolepis*$_{\mathrm{Gln}}$ had the highest ΔNSB. Therefore, the coordinated atoms are expected to affect sensitively both *acrolepis*$_{\mathrm{Wat}}$ and *acrolepis*$_{\mathrm{Gln}}$. Deep-sea fish actins had more NSB than other species at 600 bar. Since salt bridges stabilize their structures, many salt bridges which deep-sea fish actins have are expected to contribute the pressure tolerance. Although deep-sea fish actins had many salt bridges at 600 bar, *yaquinae* actin had lower NSB at 1 bar compared to rabbit actin at 1 bar. Thus, *yaquinae* actin may be optimized living in abyssal sea with many salt bridges.

Table 10. NSB including in residue-residue and residue-ATP interactions in different species.

Actin	NSB_{1bar}	NSB_{600bar}	ΔNSB
acrolepis$_{Wat}$	21.6 ± 1.9	20.0 ± 1.5	−1.6
acrolepis$_{Gln}$	19.5 ± 1.9	22.1 ± 1.5	2.6
Rabbit	24.4 ± 1.6	24.2 ± 1.7	−0.2
armatus	25.1 ± 1.4	25.7 ± 1.9	0.6
yaquinae	23.2 ± 1.5	25.1 ± 1.4	1.9

Subscripts of NSB denote simulation pressure. The ΔNSB was defined as $\Delta NSB = NSB_{600bar} - NSB_{1bar}$. These salt bridges were calculated using 40-70ns trajectories.

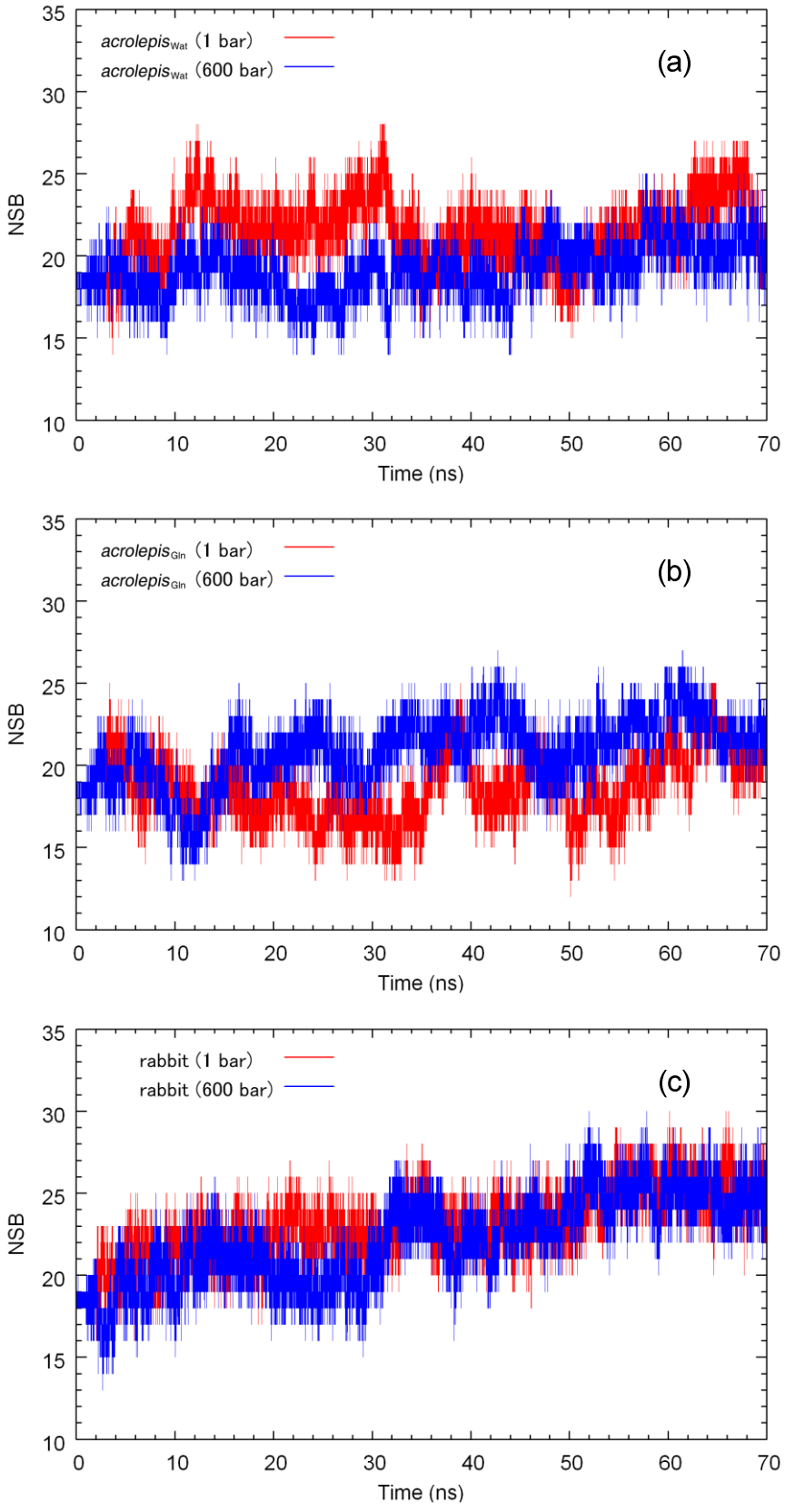
acrolepis$_{Wat}$ (1 bar)
acrolepis$_{Wat}$ (600 bar)
(a)
NSB
Time (ns)
acrolepis$_{Gln}$ (1 bar)
acrolepis$_{Gln}$ (600 bar)
(b)
NSB
Time (ns)
rabbit (1 bar)
rabbit (600 bar)
(c)
NSB
Time (ns)

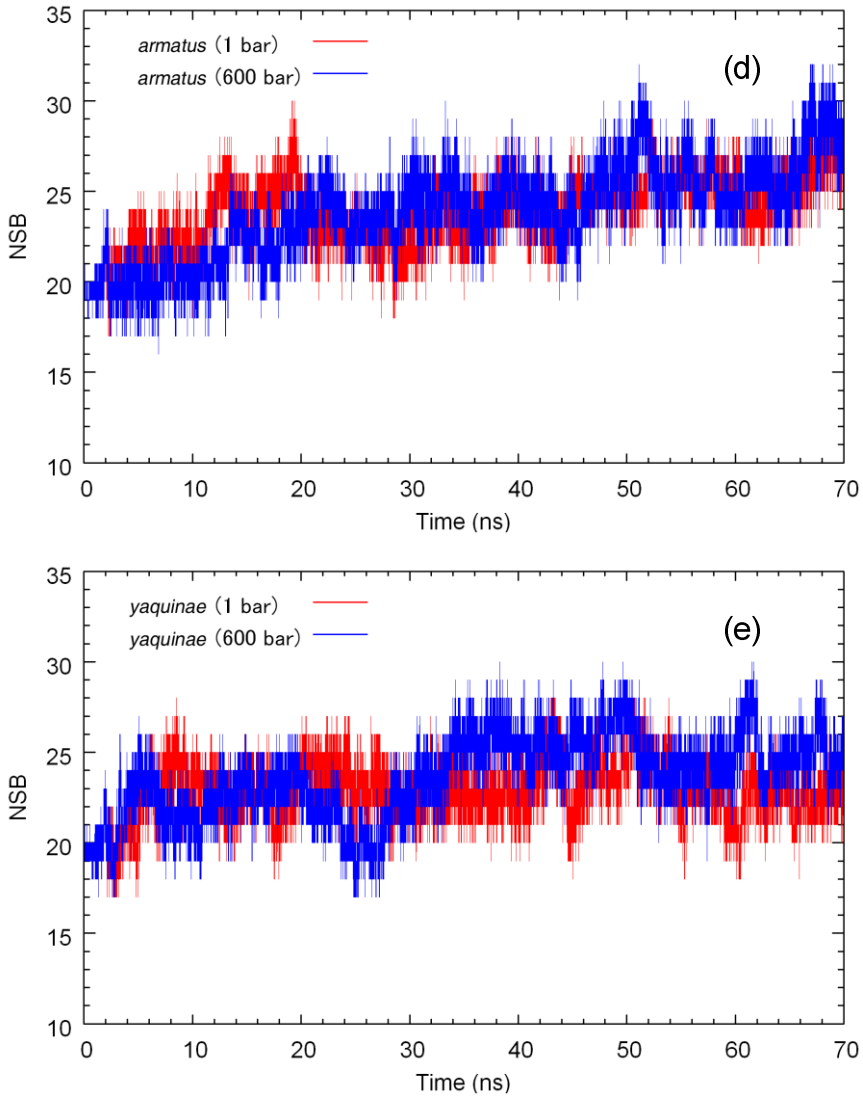

Figure 14. NSB including in residue-residue and residue-ATP interactions in different species at 1 or 600 bar.

Salt bridges between a residue and ATP were calculated to analyze the stability of ATP at the active site. ATP has nine oxygen atoms in triphosphate and these oxygen atoms can bind positive charged side-chain atoms. Oxygen atoms in ATP were distinguished from side and link oxygen atoms (Figure 12). In addition, the CHARMM22 parameter file did not discriminate charges of oxygen atom: α_1 and α_2; β_1 and β_2; γ_1, γ_2, and γ_3 (Figure 12). Since only deep-sea fish actins have Lys-137 substitution, deep-sea fish actin ATP can be bound to Lys-137 as well as Lys-18. Lys-18 bound only α- and β-side oxygen atoms in ATP whereas Lys-137 bound γ-side oxygen atoms. In other words, each link oxygen atom was not bound to lysine side-chain atoms. Almost all Lys-137 bound γ_3-side oxygen atom in the end of the active site. Therefore, Lys-137 pulled ATP to the active site and may prevent ATP dissociating at high pressure.

Table 11. Rates of salt bridge between positive side-chain atoms and oxygen atoms in ATP.

Actin	*Pressure* (bar)	Lys-18						Lys-137	Total
		O-α_1	O-α_2	O-α_3	O-β_1	O-β_2	O-β_3	O-γ	
acrolepis$_{\mathrm{Wat}}$	1	0.26	0.26	0	0.53	0.60	0	–	1.65
acrolepis$_{\mathrm{Gln}}$	1	0	0.75	0	0.86	0.57	0	–	2.18
Rabbit	1	0	1.00	0	0.63	0.94	0	–	2.57
armatus	1	0	0.97	0	0.21	0.44	0	1.19	2.81
yaquinae	1	0	0.98	0	0.14	0.95	0	1.34	3.41
acrolepis$_{\mathrm{Wat}}$	600	0	1.00	0	0.25	0.99	0	–	2.24
acrolepis$_{\mathrm{Gln}}$	600	0	1.00	0	0.46	0.97	0	–	2.43
Rabbit	600	0	1.00	0	0.45	0.88	0	–	2.33
armatus	600	1.00	0	0	0.15	0.97	0	1.25	3.37
yaquinae	600	0	0.98	0	0.55	0.06	0	0.94	2.53

A dash denotes that the salt bridge cannot be made. Oxygen atom indexes were defined as Figure 12. O-γ indicates the number of total three O-γ salt bridges.

I analyzed the combinations and positions of salt bridges to demonstrate contribution to the pressure tolerance. Both *armatus* and *yaquinae* actins at 600 bar had nine salt bridges in deep-sea fish (Table 11). Since only deep-sea fish actins had the Lys-137 substitution, deep-sea fish actins can make the K137-D154 and K137-ATP salt bridges. These salt bridges at both 1 and 600 bar were made in deep-sea fish actins and the rates were high. K359-D363 salt bridge was made at only 600 bar whereas other salt bridges can be also made at 1 bar. R37-D80 and K68-D81, R256-E195 and R196-E237 salt bridges were continuous positions along the amino acid sequence. Since atoms existing near the salt bridges were restrained, these continuous salt bridges may stabilize their local structures strongly. Only *yaquinae* and *armatus* actins at 600 bar had H275-E316 and R177-E270 salt bridges at high pressure, respectively. In addition, K84-D80 salt bridge was made in *yaquinae* and *acrolepis*$_{\mathrm{Wat}}$ actin at 600 bar. H275-E316 salt bridges connecting pairs of helices would affect stability of *yaquinae* actin at high pressure. Compared to deep-sea fish, *yaquinae* inhabits in deeper sea than *armatus*. According to the combination of salt bridges, deep-sea fish actins may selectively make salt bridges which contributed to the pressure tolerance whereas salt bridges in same secondary structures lost by conformational changes. In addition, these salt bridges mostly connected pairs of subdomains and stable secondary structures either sheet or helix. Therefore, the salt bridges would contribute to the stability of deep-sea actins.

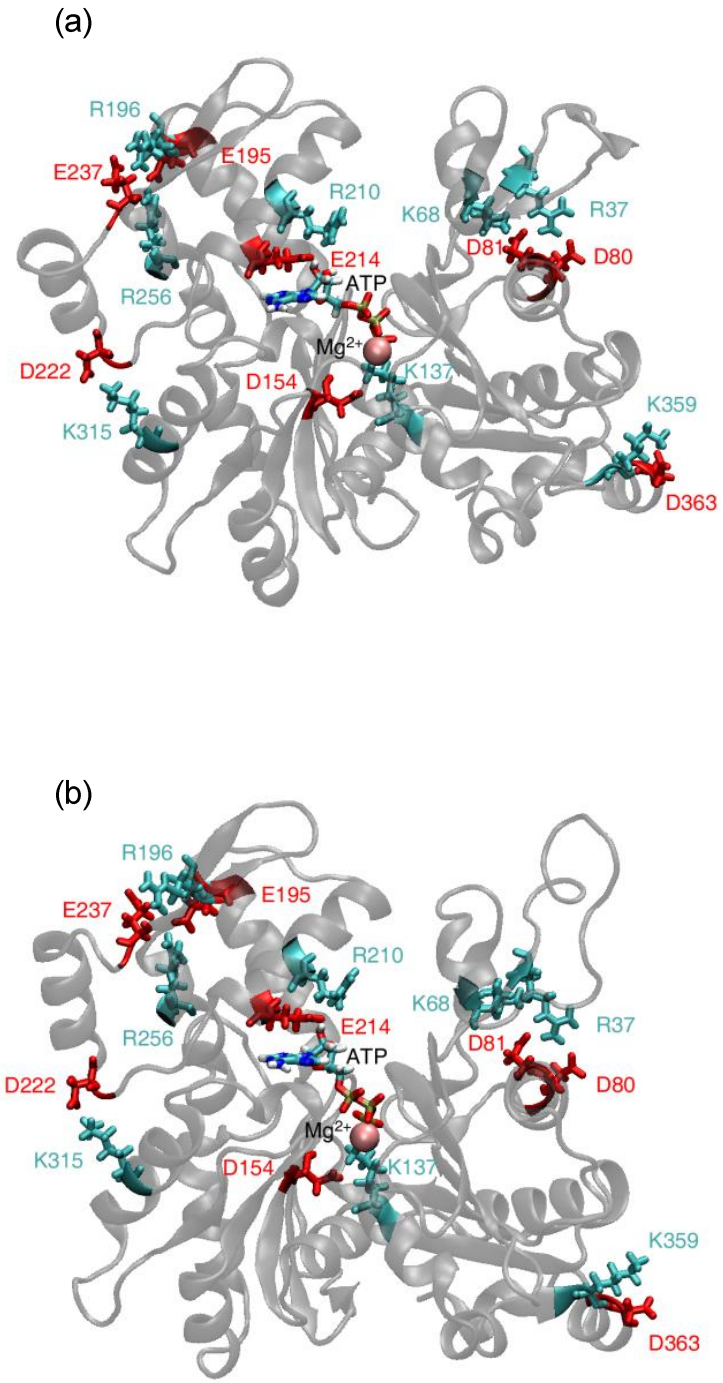

Figure 15. Salt bridges which both *armatus* and *yaquinae* had in common at 600 bar. (a) A snap shot of *armatus* actin after 70-ns simulations. (b) A snap shot of *yaquinae* actin after 70-ns simulations.

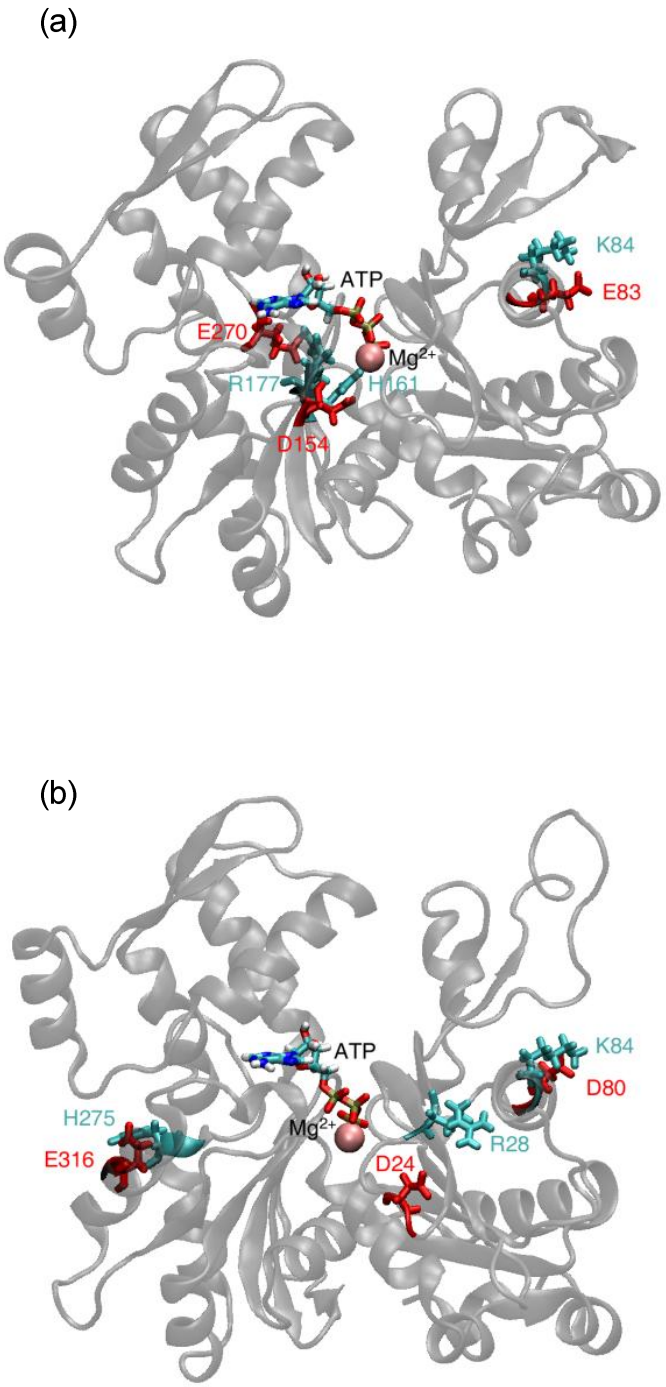

Figure 16. Salt bridges which either *armatus* or *yaquinae* had at 600 bar. (a) A snap shot of *armatus* actin after 70-ns simulations. (b) A snap shot of *yaquinae* actin after 70-ns simulations.

Table 12. Rates of salt bridges which both *armatus* and *yaquinae* had in common at 600 bar.

Salt bridge	*acro*$_{Wat}^{L}$	*acro*$_{Gln}^{L}$	Rabb^{L}	*arma*^{L}	*yaqu*^{L}	*acro*$_{Wat}^{H}$	*acro*$_{Gln}^{H}$	Rabb^{H}	*arma*^{H}	*yaqu*^{H}
R37-D80	·	1.00	0.64	1.00	0.99	1.00	·	0.99	0.79	0.99
K68-D81	·	0.61	1.00	0.86	0.91	·	·	0.89	0.99	0.54
K137-D154	–	–	–	1.00	0.96	–	–	–	1.00	1.00
K137-ATP	–	–	–	1.00	0.97	–	–	–	0.99	0.93
R196-E237	·	·	·	0.79	·	0.62	·	1.00	0.95	0.98
R210-E214	·	0.97	0.98	0.90	0.97	0.95	0.95	0.98	0.94	0.94
R256-E195	·	·	·	0.94	·	0.86	0.86	·	0.96	1.00
K315-D222	0.88	0.86	0.82	·	·	0.92	0.68	·	0.71	0.89
K359-D363	·	·	·	·	·	1.00	·	0.93	0.99	0.80

A dot and dash denote that the rate is less than 0.5 and the salt bridge cannot be made, respectively. These abbreviations *acro*$_{Wat}$, *acro*$_{Gln}$, Rabb, *arma*, and *yaqu* represent *acrolepis*$_{Wat}$, *acrolepis*$_{Gln}$, rabbit, *armatus*, and *yaquinae*, respectively. The upper subscript L and H indicate simulation pressure at 1 and 600 bar, respectively. Salt bridges which all ten species have in common were not shown.

Table 13. Rates of salt bridges which either *armatus* or *yaquinae* had at 600 bar.

Salt bridge	*acro*$_{Wat}^{L}$	*acro*$_{Gln}^{L}$	Rabb^{L}	*arma*^{L}	*yaqu*^{L}	*acro*$_{Wat}^{H}$	*acro*$_{Gln}^{H}$	Rabb^{H}	*arma*^{H}	*yaqu*^{H}
R28-D24	·	·	0.84	0.68	·	·	·	0.99	·	0.56
K84-D80	·	·	·	·	·	0.98	·	·	·	0.55
K84-E83	·	0.59	·	·	·	·	0.56	·	0.63	·
H161-D154	·	·	·	0.99	0.99	0.88	·	0.81	1.00	·
R177-E270	·	·	0.95	·	·	·	·	·	0.98	·
H275-E316	·	0.70	0.92	1.00	1.00	·	·	·	·	1.00

Same as in Table 12.

Table 14. Rates of salt bridges which neither *armatus* nor *yaquinae* hade at 600 bar.

Salt bridge	*acro*$_{Wat}^{L}$	*acro*$_{Gln}^{L}$	Rabb^{L}	*arma*^{L}	*yaqu*^{L}	*acro*$_{Wat}^{H}$	*acro*$_{Gln}^{H}$	Rabb^{H}	*arma*^{H}	*yaqu*^{H}
K18-D11	0.72	0.69	·	0.84	·	·	·	·	·	·
K50-D51	·	·	·	·	·		·	0.62	·	·
K50-E57	0.80	0.92	·	·	·	0.72	·	·	·	·
K68-E72	·	·	·	·	·	·	0.85	·	·	·
H73-E72	·	0.83	·	·	·	·	·	·	·	·
K84-D51	·	·	0.71	·	·	·	·	·	·	·
H88-E93	0.56	·	·	·	·	·	·	·	·	·
K113-E117	·	·	0.89	·	·	·	·	·	·	·
K191-E195	·	·	0.81	·	·	·	·	0.74	·	·
K291-D288	·	·	0.60	·	·	·	·	·	·	·
K291-D292	0.95	·	0.96	0.95	0.96	·	0.50	0.98	·	·

Same as in Table 12.

Table 15. Details of salt bridge combinations about subdomains and secondary structures.

(a)

Salt bridge	Sub-Sub	Structure
R37-D80	2-1	Sheet-Helix
K68-D81	2-1	Sheet-Helix
K137-D154	1-3	Helix-Sheet
K137-ATP	–	–
R196-E237	4-4	Helix-Loop
R210-E214	4-4	Same helix
R256-E195	4-4	Helix-Helix
K315-D222	3-4	Helix-Helix
K359-D363	1-1	Same helix

(b)

Salt bridge	Sub-Sub	Structure
R28-D24	1-1	Same loop
K84-D80	1-1	Same helix
K84-E83	1-1	Same helix
H161-D154	3-3	Sheet-Sheet
R177-E270	3-3	Sheet-Loop
H275-E316	3-3	Helix-Helix

(c)

Salt bridge	Sub-Sub	Structure
K18-D11	1-1	Sheet-Sheet
K50-D51	2-2	Loop-Helix
K50-E57	2-2	Loop-Helix
K68-E72	2-1	Sheet-Sheet
H73-E72	1-1	Same loop
K84-D51	1-2	Helix-Sheet
H88-E93	1-1	Helix-Loop
K113-E117	1-1	Same helix
K191-E195	4-4	Same helix
K291-D288	3-3	Same helix
K291-D292	3-3	Same helix

(a) Combinations of salt bridges which both *armatus* and *yaquinae* had in common at 600 bar. Sub-Sub denotes the subdomain number of positive charged and negative charged residue. Structure indicates the secondary structure of positive charged and negative charged residue excluding from same secondary structures. (b) Same as (a) but either *armatus* or *yaquinae* had. (c) Same as (a) but neither *armatus* nor *yaquinae* had.

Table 16. The number of salt bridges in combinations.

Actin	Different secondary structures	Different subdomains	Side-chain and ATP	Others
acrolepis$_{\mathrm{Wat}}$	5	2	0	5
acrolepis$_{\mathrm{Gln}}$	3	2	0	3
Rabbit	4	2	0	6
armatus	6	4	1	4
yaquinae	6	4	1	4

The salt bridges were counted excluded in salt bridges which all species have in common. These salt bridges were calculated using 40-70ns trajectories.

Most of salt bridges which both *armatus* and *yaquinae* had in common at 600 bar were formed between the residues distant along the amino acid sequence whereas salt bridges which neither *armatus* nor *yaquinae* have at 600 bar were formed between adjacent residues or near residues. Therefore, deep-sea fish actin had salt bridges which would affect stability of actin structures.

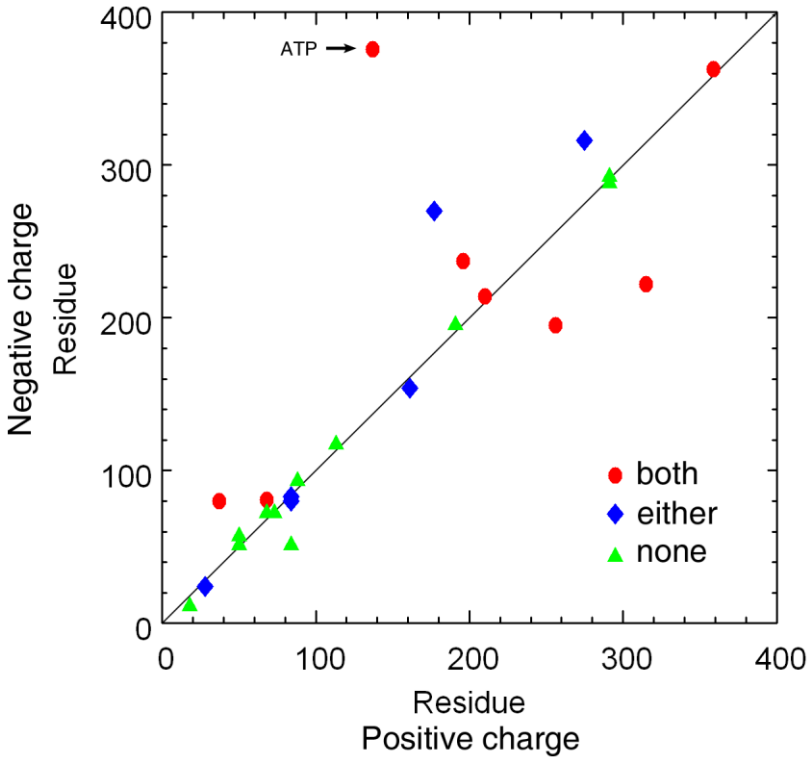

Figure 17. Salt bridge combinations between positive charged and negative charged residues. A circle (●), lozenge (◆), and triangle (▲) denote salt bridges which both *armatus* and *yaquinae*, either *armatus* or *yaquinae*, and neither *armatus* nor *yaquinae* had at 600 bar, respectively. I regarded ATP as a residue on the position 376.

Deep-sea fish actins had salt bridges K137-D154 and R210-E214 at initial states. At the beginning of the simulations, the distance between K137 and

ATP decreased quickly and then K137-ATP salt bridge was made. Since Lys-137 is a substitution residue, this conformational change would be induced by K137-D154 salt bridges. The decrease of these distances may occur at active site and then salt bridges on the surface of protein were formed.

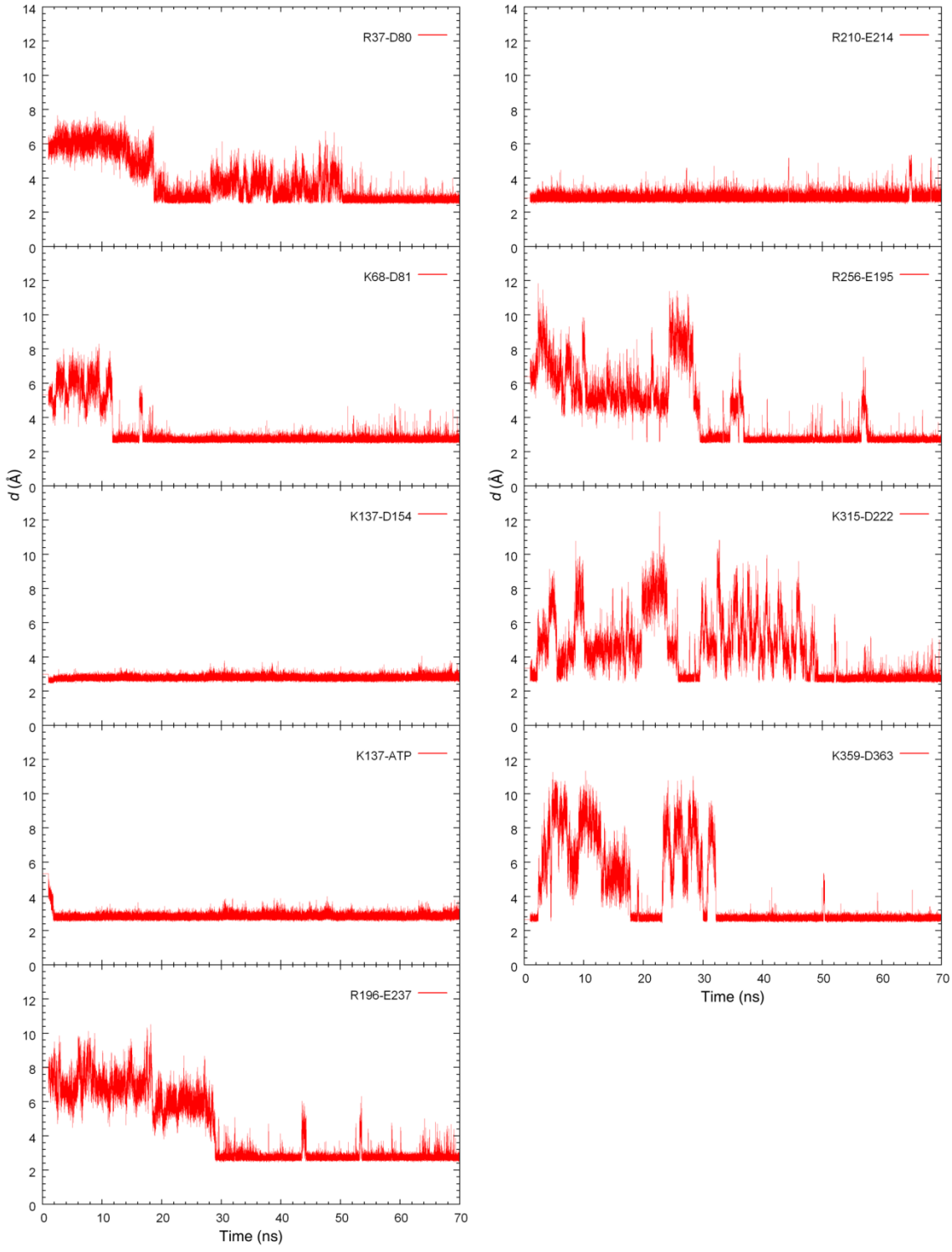

Figure 18. Distances of salt bridges specific to deep-sea fish in *armatus* actin had at 600 bar.

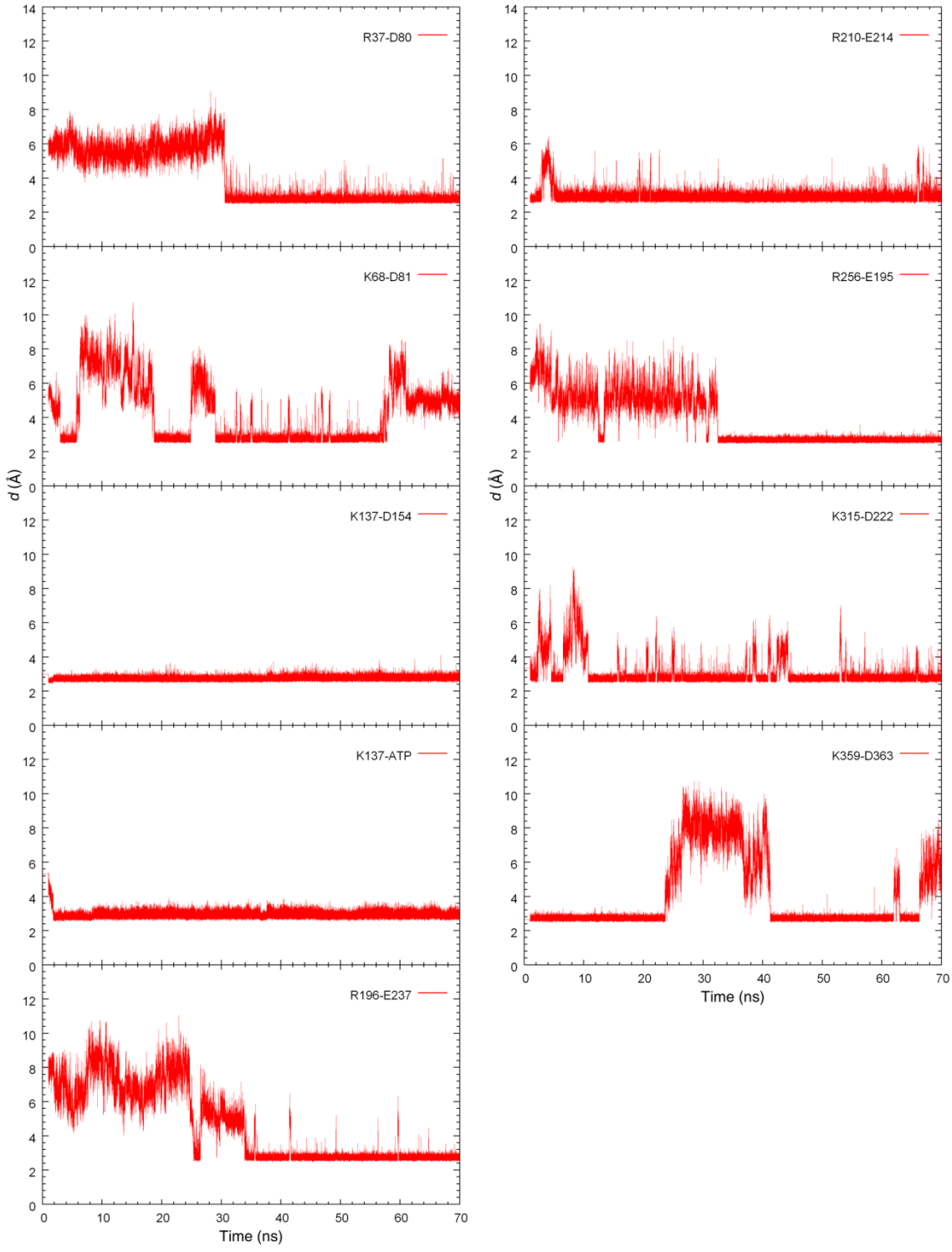

Figure 19. Distances of salt bridges specific to deep-sea fish in *yaquinae* actin had at 600 bar.

4 Perspectives

Although the change of CN for Mg^{2+} was not observed in this study, high pressure probably has some effects on the active site. I did not observe significant change of the coordinated atoms and these distances although some coordinated atom positions are slightly different. However, effect of the ligands and residues at the active site can be analyzed using the solvation free energy. I will carry out the simulations in the solution system and reference system including in pure solvent and the solute structure. These MD simulations provide the histogram of solute-solvent interaction energy for both of these systems. The solvent free energy was calculated with combining two systems. I expect that high pressure affect the solvent free energy. In other words, the solvent free energy would demonstrate the increase of dissociating rate for ligands induced by the high pressure.

In this study, I performed simulations using G-actin to analyze their stability. In addition to G-actin, I will carry out the simulations with F-actin. Since some F-actin structures have been solved at high resolutions recently [8; 9; 10; 11], I can obtain the initial coordinates of F-actin for MD simulations. Although all atom coordinates of F-actin are still unclear, I will carry out structure modeling of F-actin using some F- and G-actin structures. All-atom MD simulations will be carried out after the modeling of F-actin. In the modeling the F-actin structures, it is important to choose the length of filament. I can estimate appropriate length using the mechanism of polymerization and F-actin structures. To begin the elongation of filament, a nucleotide nucleus is needed. The smallest size is known to be actin trimer [48]. When four or more actins aggregate, polymerization will start with ATP

hydrolysis [9]. Therefore, four or longer promoters are needed for MD simulations. On the other hand, F-actin is a helical structure and the half period of the helix is about 13 actins [8]. Since I perform MD simulations with periodic boundary conditions, it is sufficient to run with the half period of F-actins. Consequently, I suggest that the system should have F-actin including in 4-13 actins. Through MD simulation using F-actin, I would analyze the dynamics of actin and the reaction of ATP hydrolysis. Since F-actin is known to have polymorphism [10], I may observe some modes of F-actin. To elucidate the essence of dynamics in actin, I will perform the all-atom MD simulations.

5 Conclusions

I analyzed the structures of actins obtained from the species living in deep-sea, shallow water, and land at atmospheric and high pressure. High pressure has been shown to induce V_{ex} decrease and SASA increase in many species at 600 bar by MD simulations. Although differences between species were relatively small in V_{ex} and SASA changes, PMOI showed a notable difference. The 1st PMOI increased at high pressure in species living in land or shallow water. However, deep-sea fish actins were not significantly affected by high pressures in each PMOI. Therefore, the disciform structures of actin living in land or shallow water were transformed to be thinner induced in high pressure. On the other hand, deep-sea fish actin may be less affected in high pressure.

Dihedral angles between subdomains were twisted at high pressure although distances between subdomains were not changed. Only *yaquinae* inhabiting in the deepest sea had more flat form than other species had. However, notable value which both *yaquinae* and *armatus* actins have in common did not exist.

A divalent cation such as Mg^{2+} assists ATP hydrolysis during the elongation of filament. It was coordinated with six oxygen atoms included in ATP, water molecules, and a Gln-137 side-chain atom. Although previous study showed that high pressure induced dissociating of ligands [20], the CN for Mg^{2+} did not change in MD simulations. Moreover, atoms coordinated to Mg^{2+} were not replaced and the distance between Mg^{2+} and a coordinated atom was not changed significantly. Since CN was not changed, transitions between binding ligands and releasing ligands in actin would be hindered by

energy barriers.

Salt bridge analysis showed a lot of information on whole structures and local structures such as the active site. Deep-sea fish actins have more NSB than other species at high pressure although rabbit actin had more NSB than *yaquinae* at atmospheric pressure. Thus, deep-sea fish actins, in particularly *yaquinae* actin, probably needed high pressure to change them into more pressure-adaptive structures. In the active site, only deep-sea fish actins had a salt bridge between Lys-137 side-chain atom and γ-oxygen atom in ATP although all species had a salt bridge between Lys-18 side-chain atom and α- or β-side oxygen atom in ATP. Previous study showed increase of the ligands dissociation rate in actin living in land or shallow water at high pressure [20]. In other words, these actins cannot hold ligands at high pressure. On the other hand, Lys-137 substitution located at the end of the active site in deep-sea fish actin. This residue pulled the ATP and may prevent ATP dissociation from the active site. Therefore, the salt bridge that deep-sea fish actins only have may play a role to maintain ATP at the active site even at high pressure.

Deep-sea fish actins have nine salt bridges common in both *armatus* and *yaquinae* at 600 bar excluding the salt bridges common in all the species. Both *armatus* and *yaquinae* actins had salt bridges which mostly connected pairs of stable secondary structures (i.e., helix or sheet). Two pairs of stable salt bridges (i.e., R37-D80 and K68-D81, R256-E195 and R196-E237) may affect local stability of actins. In addition, some salt bridges also connect different subdomains. These salt bridges are formed between the residues distant along the amino acid sequence whereas nearer residues along the

sequence do not form salt bridges in neither *armatus* nor *yaquinae* at 600 bar. Consequently, the salt bridges would stabilize deep-sea fish actins at high pressure. Deep-sea fish actins lost the salt bridges within secondary structures and acquired new salt bridges which stabilize the interaction between different secondary structures as well as different subdomains at high pressure.

Deep-sea fish actins have many salt bridges at the active site and secondary structures. The salt bridges probably connect between residues or residue and ligand atom effectively. Therefore, these salt bridges would be a key for the mechanism of the pressure tolerance and enable deep-sea fish actins to inhabit in abyssal sea.

6 Acknowledgements

I genuinely thank Prof. Akio Kitao for his courteous supervision and generous guidance. I have obtained plenty of advice through great discussion with him. In addition, his encouragement helps me to advance in study. I would like to thank all Kitao laboratory past and present members. In particularly, I am really grateful to Dr. Kuzuhiro Takemura for daily countenance. I owe him a debt of gratitude for his lavish technical support of software, hardware, and others. I appreciate Dr. Yasutaka Nishihara for technical support of clusters and servers. His advice through discussion greatly benefited my study. I wish to thank Dr. Shun Sakuraba for programming and his sound advice. Finally, I thank Mr. Yu Yamamori and Mr. Ryuhei Harada to daily support and exiting discussion.

References

1. Herman, I. M. (1993). Actin isoforms. *Current Opinion in Cell Biology* 5, 48-55.
2. Pollard, T. D. & Borisy, G. G. (2003). Cellular motility driven by assembly and disassembly of actin filaments. *Cell* 112, 453-465.
3. Su, Y., Kondrikov, D. & Block, E. R. (2007). Beta-Actin: A Regulator of NOS-3. *Science Signaling* 2007, 52-54.
4. Belyantseva, I. A., Perrin, B. J., Sonnemann, K. J., Zhu, M., Stepanyan, R., McGee, J., Frolenkov, G. I., Walsh, E. J., Friderici, K. H., Friedman, T. B. & Ervasti, J. M. (2009). gamma-Actin is required for cytoskeletal maintenance but not development. *Proceedings of the National Academy of Sciences of the United States of America* 106, 9703-9708.
5. Furness, D. N., Katori, Y., Mahendrasingam, S. & Hackney, C. M. (2005). Differential distribution of beta- and gamma-actin in guinea-pig cochlear sensory and supporting cells. *Hearing Research* 207, 22-34.
6. Karakozova, M., Kozak, M., Wong, C. C. L., Bailey, A. O., Yates, J. R., Mogilner, A., Zebroski, H. & Kashina, A. (2006). Arginylation of beta-actin regulates actin cytoskeleton and cell motility. *Science* 313, 192-196.
7. Kabsch, W., Mannherz, H. G., Suck, D., Pai, E. F. & Holmes, K. C. (1990). ATOMIC-STRUCTURE OF THE ACTIN - DNASE-I COMPLEX. *Nature* 347, 37-44.
8. Oda, T., Iwasa, M., Aihara, T., Maeda, Y. & Narita, A. (2009). The nature of the globular-to fibrous-actin transition. *Nature* 457, 441-445.
9. Murakami, K., Yasunaga, T., Noguchi, T. Q. P., Gomibuchi, Y., Ngo, K. X., Uyeda, T. Q. P. & Wakabayashi, T. (2010). Structural Basis for Actin Assembly, Activation of ATP Hydrolysis, and Delayed Phosphate Release. *Cell* 143, 275-287.

10. Galkin, V. E., Orlova, A., Schroder, G. F. & Egelman, E. H. (2010). Structural polymorphism in F-actin. *Nature Structural & Molecular Biology* 17, 1318-U169.

11. Fujii, T., Iwane, A. H., Yanagida, T. & Namba, K. (2010). Direct visualization of secondary structures of F-actin by electron cryomicroscopy. *Nature* 467, 724-729.

12. Pfaendtner, J., Lyman, E., Pollard, T. D. & Voth, G. A. (2009). Structure and Dynamics of the Actin Filament. *Journal of Molecular Biology* 396, 252-263.

13. Schutt, C. E., Myslik, J. C., Rozycki, M. D., Goonesekere, N. C. W. & Lindberg, U. (1993). THE STRUCTURE OF CRYSTALLINE PROFILIN BETA-ACTIN. *Nature* 365, 810-816.

14. Arber, S., Barbayannis, F. A., Hanser, H., Schneider, C., Stanyon, C. A., Bernard, O. & Caroni, P. (1998). Regulation of actin dynamics through phosphorylation of cofilin by LIM-kinase. *Nature* 393, 805-809.

15. Humphrey, W., Dalke, A. & Schulten, K. (1996). VMD: Visual molecular dynamics. *Journal of Molecular Graphics* 14, 33-38.

16. Carlier, M. F., Pantaloni, D. & Korn, E. D. (1986). FLUORESCENCE MEASUREMENTS OF THE BINDING OF CATIONS TO HIGH-AFFINITY AND LOW-AFFINITY SITES ON ATP-G-ACTIN. *Journal of Biological Chemistry* 261, 778-784.

17. Carlier, M. F. & Pantaloni, D. (2007). Control of actin assembly dynamics in cell motil. *Journal of Biological Chemistry* 282, 23005-23009.

18. Ikeuchi, Y., Suzuki, A., Oota, T., Hagiwara, K., Tatsumi, R., Ito, T. & Balny, C. (2002). Fluorescence study of the high pressure-induced denaturation of skeletal muscle actin. *European Journal of Biochemistry* 269, 364-371.

19. Ikkai, T. & Ooi, T. (1966). The effects of Pressure on F-G Transformation of Actin. *Biochemistry* 5, 1551-1560.

20. Morita, T. (2003). Structure-based analysis of high pressure adaptation of alpha-actin. *Journal of Biological Chemistry* 278, 28060-28066.

21. Morita, T. (2008). Comparative sequence analysis of myosin heavy chain proteins from congeneric shallow- and deep-living rattail fish (genus Coryphaenoides). *Journal of Experimental Biology* 211, 1362-1367.

22. Siebenaller, J. F. & Somero, G. N. (1979). PRESSURE-ADAPTIVE DIFFERENCES IN THE BINDING AND CATALYTIC PROPERTIES OF MUSCLE-TYPE (M4) LACTATE-DEHYDROGENASES OF SHALLOW-LIVING AND DEEP-LIVING MARINE FISHES. *Journal of Comparative Physiology* 129, 295-300.

23. Siebenaller, J. F. (1984). PRESSURE-ADAPTIVE DIFFERENCES IN NAD-DEPENDENT DEHYDROGENASES OF CONGENERIC MARINE FISHES LIVING AT DIFFERENT DEPTHS. *Journal of Comparative Physiology* 154, 443-448.

24. Vorobiev, S., Strokopytov, B., Drubin, D. G., Frieden, C., Ono, S., Condeelis, J., Rubenstein, P. A. & Almo, S. C. (2003). The structure of nonvertebrate actin: Implications for the ATP hydrolytic mechanism. *Proceedings of the National Academy of Sciences of the United States of America* 100, 5760-5765.

25. Iwasa, M., Maeda, K., Narita, A., Maeda, Y. & Oda, T. (2008). Dual roles of Gln(137) of actin revealed by recombinant human cardiac muscle alpha-actin mutants. *Journal of Biological Chemistry* 283, 21045-21053.

26. Imai, T. & Sugita, Y. (2010). Dynamic Correlation between Pressure-Induced Protein Structural Transition and Water Penetration. *Journal of Physical Chemistry B* 114, 2281-2286.

27. Collins, M. D., Hummer, G., Quillin, M. L., Matthews, B. W. & Gruner, S. M. (2005). Cooperative water filling of a nonpolar protein cavity observed by high-pressure

crystallography and simulation. *Proceedings of the National Academy of Sciences of the United States of America* 102, 16668-16671.

28. Grigera, J. R. & McCarthy, A. N. (2010). The Behavior of the Hydrophobic Effect under Pressure and Protein Denaturation. *Biophysical Journal* 98, 1626-1631.

29. Sarupria, S., Ghosh, T., Garcia, A. E. & Garde, S. (2010). Studying pressure denaturation of a protein by molecular dynamics simulations. *Proteins-Structure Function and Bioinformatics* 78, 1641-1651.

30. Busa, J., Hayryan, S., Hu, C. K., Skrivanek, J. & Wu, M. C. (2010). CAVE: A package for detection and quantitative analysis of internal cavities in a system of overlapping balls: Application to proteins. *Computer Physics Communications* 181, 2116-2125.

31. Hirata, K., Muraoka, S., Suenaga, K., Kuroda, T., Kato, K., Tanaka, H., Yamamoto, M., Takata, M., Yamada, K. & Kigoshi, H. (2006). Structure basis for antitumor effect of aplyronine A. *Journal of Molecular Biology* 356, 945-954.

32. Morton, W. M., Ayscough, K. R. & McLaughlin, P. J. (2000). Latrunculin alters the actin-monomer subunit interface to prevent polymerization. *Nature Cell Biology* 2, 376-378.

33. Jorgensen, W. L., Chandrasekhar, J. & Madura, J. D. (1983). Comparison of simple potential functions for simulating liquid water. *Journal of Chemical Physics* 79(2), 926-636.

34. Wriggers, W. & Schulten, K. (1999). Investigating a back door mechanism of actin phosphate release by steered molecular dynamics. *Proteins-Structure Function and Genetics* 35, 262-273.

35. MacKerell, A. D., Banavali, N. & Foloppe, N. (2000). Development and current status of the CHARMM force field for nucleic acids. *Biopolymers* 56, 257-265.

36. Wu, Y. J., Tepper, H. L. & Voth, G. A. (2006). Flexible simple point-charge water model with improved liquid-state properties. *Journal of Chemical Physics* 124.

37. Phillips, J. C., Braun, R., Wang, W., Gumbart, J., Tajkhorshid, E., Villa, E., Chipot, C., Skeel, R. D., Kale, L. & Schulten, K. (2005). Scalable molecular dynamics with NAMD. *Journal of Computational Chemistry* 26, 1781-1802.

38. Kell, G. S. (1967). PRECISE REPRESENTATION OF VOLUME PROPERTIES OF WATER AT 1 ATMOSPHERE. *Journal of Chemical and Engineering Data* 12, 66-69.

39. Essmann, U., Perera, L., Berkowitz, M. L., Darden, T., Lee, H. & Pedersen, L. G. (1995). A SMOOTH PARTICLE MESH EWALD METHOD. *Journal of Chemical Physics* 103, 8577-8593.

40. Darden, T., York, D. & Pedersen, L. (1993). PARTICLE MESH EWALD - AN N.LOG(N) METHOD FOR EWALD SUMS IN LARGE SYSTEMS. *Journal of Chemical Physics* 98, 10089-10092.

41. Feller, S. E., Zhang, Y. H., Pastor, R. W. & Brooks, B. R. (1995). CONSTANT-PRESSURE MOLECULAR-DYNAMICS SIMULATION - THE LANGEVIN PISTON METHOD. *Journal of Chemical Physics* 103, 4613-4621.

42. Hoover, W. G. (1986). CONSTANT-PRESSURE EQUATIONS OF MOTION. *Physical Review A* 34, 2499-2500.

43. Ryckaert, J. P., Ciccotti, G. & C., B. H. J. (1977). Numerical Integration of the Cartesian Equations of Motion of a System with Constraints: Molecular Dynamics of n-Alkanes. *Journal of Computational Physics* 23, 327-341.

44. Miyamoto, S. & Kollman, P. A. (1992). SETTLE - AN ANALYTICAL VERSION OF THE SHAKE AND RATTLE ALGORITHM FOR RIGID WATER MODELS. *Journal of Computational Chemistry* 13, 952-962.

45. Rashin, A. A. (1984). BURIED SURFACE-AREA, CONFORMATIONAL ENTROPY,

AND PROTEIN STABILITY. *Biopolymers* 23, 1605-1620.

46. Ikeda, T., Boero, M. & Terakura, K. (2007). Hydration properties of magnesium and calcium ions from constrained first principles molecular dynamics. *Journal of Chemical Physics* 127.

47. Yu, I., Tasaki, T., Nakada, K. & Nagaoka, M. (2010). Influence of Hydrostatic Pressure on Dynamics and Spatial Distribution of Protein Partial Molar Volume: Time-Resolved Surficial Kirkwood-Buff Approach. *Journal of Physical Chemistry B* 114, 12392-12397.

48. Sept, D. & McCammon, J. A. (2001). Thermodynamics and kinetics of actin filament nucleation. *Biophysical Journal* 81, 667-674.